UNLV University Libraries
University of Nevada, Las Vegas

UNLV Theses, Dissertations, Professional Papers, and Capstones

8-2010

Vibrational spectroscopic study of the 1,3,5,7-cyclooctatetraene at high static pressures

Edward Romano
University of Nevada, Las Vegas

Follow this and additional works at: https://digitalscholarship.unlv.edu/thesesdissertations

Part of the Atomic, Molecular and Optical Physics Commons, and the Organic Chemistry Commons

Repository Citation

Romano, Edward, "Vibrational spectroscopic study of the 1,3,5,7-cyclooctatetraene at high static pressures" (2010). *UNLV Theses, Dissertations, Professional Papers, and Capstones*. 850.
https://digitalscholarship.unlv.edu/thesesdissertations/850

This Thesis is protected by copyright and/or related rights. It has been brought to you by Digital Scholarship@UNLV with permission from the rights-holder(s). You are free to use this Thesis in any way that is permitted by the copyright and related rights legislation that applies to your use. For other uses you need to obtain permission from the rights-holder(s) directly, unless additional rights are indicated by a Creative Commons license in the record and/or on the work itself.

This Thesis has been accepted for inclusion in UNLV Theses, Dissertations, Professional Papers, and Capstones by an authorized administrator of Digital Scholarship@UNLV. For more information, please contact digitalscholarship@unlv.edu.

VIBRATIONAL SPECTROSCOPIC STUDY OF 1,3,5,7-CYCLOOCTATETRAENE AT HIGH STATIC PRESSURES

by

Edward Don Romano

Bachelor of Science
University of Nevada Las Vegas
2007

A thesis submitted in partial fulfillment
of the requirements for

Master of Science Degree in Physics
Department of Physics
College of Sciences

Graduate College
University of Nevada Las Vegas
August 2010

Copyright by Edward Don M. Romano 2010
All Rights Reserved

THE GRADUATE COLLEGE

We recommend the thesis prepared under our supervision by

Edward Don Romano

entitled

Vibrational Spectroscopic Study of the 1,3,5,7-Cyclooctatetraene at High Static Pressures

be accepted in partial fulfillment of the requirements for the degree of

Master of Science in Physics

Michael Pravica, Committee Co-chair

Lon Spight, Committee Co-chair

Oliver Tschauner, Committee Member

Len Zane, Committee Member

Clemens Heske, Graduate Faculty Representative

Ronald Smith, Ph. D., Vice President for Research and Graduate Studies
and Dean of the Graduate College

August 2010

ABSTRACT

Vibrational Spectroscopic Study of 1,3,5,7-Cyclooctatetraene at High Static Pressures

by

Edward Romano

Dr. Michael Pravica, Examination Committee Chair
Associate Professor of Physics
University of Nevada, Las Vegas

1,3,5,7-cyclooctatetraene (COT) is a single-ringed hydrocarbon that has not been studied extensively under high static pressures. It was the intent of this study to reveal its high-pressure behavior through its vibrational spectra. To this end, its infrared spectra as a function of pressure were collected at the National Synchrotron Light Source (NSLS) U2A beamline, as well as its Raman spectra over pressure using a micro-Raman spectrometer.

The spectra show the typical stiffening of force constants with increasing pressure for most peaks, particularly those which would theoretically exhibit a mode-softening behavior under hypotheses of molecular planarization and aromatization. Additionally, the data supports the findings of a previous spectroscopic study done by our group, in which the sample transforms into a phase lacking long-range order and possessing a waxy appearance upon release of the sample from pressure, indicative of high-pressure induced chemistry.

TABLE OF CONTENTS

ABSTRACT.....iii

LIST OF FIGURES.....v

ACKNOWLEDGEMENTS.....vii

CHAPTER 1 INTRODUCTION AND BACKGROUND.....1
1,3,5,7-Cyclooctatetraene (COT).....1
High-Pressure Spectroscopy.....4
Measurement of Pressure: Ruby.....4
Vibrational Spectroscopy.....5
Raman Spectroscopy.....8
Infrared Spectroscopy.....9
FT-IR.....10
The Michelson Interferometer.....12
Detectors.....14
Synchrotron Radiation.....15

CHAPTER 2 EXPERIMENTAL PROCEDURES.....17
High-Pressure Generation.....17
Infrared Experiment.....21
Raman Experiment.....25

CHAPTER 3 RESULTS.....27
The Pressure (X) Axis.....27
The Wavenumber (Y) Axis.....30
Discussion.....37
Flattening.....37
Aromaticity.....40
Phase transition.....45
CHAPTER 4 CONCLUSIONS.....51

REFERENCES.....53

VITA.....55

LIST OF FIGURES

Figure 1 Tub Structure of COT....1
Figure 2 Crystal Structure of COT at 129 K [1]....2
Figure 3 Illustration of the COT molecule "flattening" into a planar configuration. Modified from [2]....3
Figure 4 Ruby luminescence energy level diagram [14]....5
Figure 5 Diagram of a Michelson interferometer....12
Figure 6 A Merrill-Bassett 3-pinned DAC was used for the Raman measurements....17
Figure 7 Symmetric type cell was used for the IR measurements....17
Figure 8 Diamond mounting jig....18
Figure 9 Electronic Discharge Machine (EDM)....18
Figure 10 Schematic of the U2A beamline setup [21]. Microscope 1 was used for the MidIR experiments and Microscope 3 for the FarIR....23
Figure 11 Schematic of the micro-Raman setup [23]....26
Figure 12 A rough fit of the Ruby R1 and R2 peaks with Lorentzian profiles at P~7 GPa....28
Figure 13 An example of the locally fitted background. The leftmost unstarred peak is fitted to a Lorentzian to a better extract the positions of the 2 overlapping (starred) vibrational modes....28
Figure 14 MidIR vibrational spectra raw data stackplot....33
Figure 15 FarIR vibrational spectra data stackplot....34
Figure 16 Raman vibrational spectra data stackplot 1. Grating centered around 668 nm....35
Figure 17 Raman vibrational spectra data stackplot 2. Grating centered around 690 nm....36
Figure 18 Raman vibrational spectra data stackplot 3. Grating centered around 725 nm....36
Figure 19 C-H op bending mode region (MidIR)....38
Figure 20 C-H op bending + C-C stretching mode region (MidIR)....38
Figure 21 C-H ip bending mode; C-H op bend. + C-C stretch (MidIR)....39
Figure 22 C=C stretching region (Raman)....39
Figure 23 C=C stretch region (MidIR)....41
Figure 24 FarIR region....42
Figure 25 Low-frequency region (Raman)....42
Figure 26 C-H stretching region (MidIR)....43
Figure 27 C-H ip bending mode (MidIR)....44
Figure 28 Unassigned region (MidIR)....44
Figure 29 Correlation Table for low-temp phase of COT. Modes of E symmetry are split by the presence of the C_2 site symmetry....46
Figure 30 FarIR spectrum at 0.38 GPa....48
Figure 31 FarIR spectrum at ~10 GPa....48
Figure 32 Entire MidIR spectrum upon compression to 1.59 GPa....49

Figure 33 Entire MidIR spectrum upon decompression to 1.05 GPa.....49
Figure 34 C-H stretch region IR spectrum of benzene over pressure. a) Benzene under compression. b) Benzene under decompression. Modified from [28].....50

ACKNOWLEDGEMENTS

I would first like to thank the people who were directly involved with this thesis:

Dr. Sergey Tkachev, who served as my greatest guide through the course of this work
Marty Galley, who took the great majority of the data on the Raman spectra over pressure
Brian Yulga, who has been a wealth of answers to my many questions
Dr. Zhenxian Liu, for his help in learning how to operate the U2A setup at the NSLS
Brian Hostermann, for his help in learning how to operate his micro-Raman system
Eunja Kim, for providing me with a valuable resource in her knowledge of group theory
Ravhi Kumar, for being a welcoming resource with regards to the data analysis

And my committee members:
Dr. Lon Spight, for his sage advice and friendly guidance
Dr. Oliver Tschauner, for sharing his bottomless depth of knowledge of the field
Dr. Clemens Heske, for his valuable insight into the interpretation of the data
Dr. Len Zane, for inspiring me to really understand what I'm doing
Dr. Michael Pravica, my adviser, for his efforts to see my thesis project to completion and for the many lessons he taught me about research

I would be remiss to not include my fellow peers in the graduate program, especially those who worked in HiPSEC and have grown up in the field with me. Special mention goes to Boki, Zveki, and Rasta. And the rest of the Physics faculty, for nurturing an academic environment through which I came into my own as a life-long student of science in general and physics in particular.

CHAPTER 1

INTRODUCTION AND BACKGROUND

1,3,5,7-Cyclooctatetraene (COT)

COT (C_8H_8) is an organic molecule consisting of an 8-member carbon ring with alternating double bonds with one hydrogen atom linked to each carbon vertex. The molecule has a "tub" structure (D_{2d} symmetry) in which the angle between an adjacent single and double bond is not 135°, as it would be for a planar octagon. This structure is presented in Figure 1. COT is liquid at ambient conditions, and crystallizes at 129 K and room pressure (~0 GPa) into an orthorhombic structure with space group Aba2. The unit cell is shown in Figure 2. The lattice parameters are a=7.664(6) Å, b=7.650(3) Å, and c=10.688(6) Å [1].

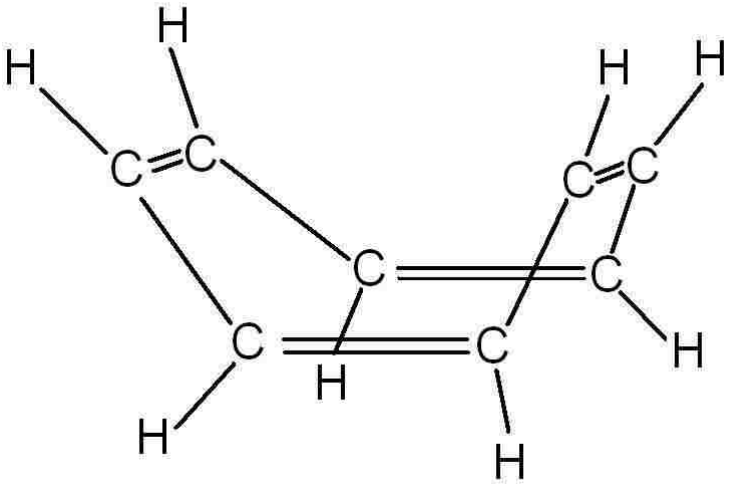

Figure 1. *Tub structure of COT.*

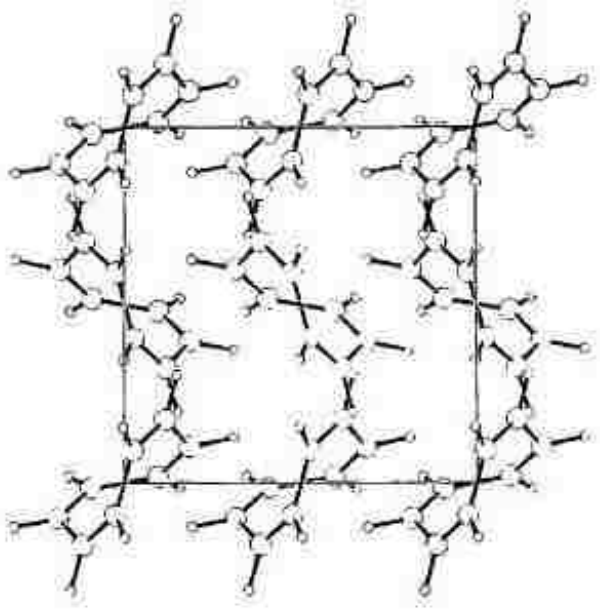

Figure 2. *Crystal structure of COT at 129 K (taken from [1]).*

COT is a relatively simple organic molecule, and it has a nonplanar structure that this work hypothesizes to be reversible under high static pressures. That is, it is a goal of this thesis to examine whether or not the molecule undergoes a "flattening" under pressure, in which the COT molecule transforms from a tub-shaped conformation to a planar one. This would hypothetically occur via a decrease of the extra-planar angles with pressure. An illustration of this planarization is given by Figure 3 (showing COT from the side, with the principal axis pointing up the page), where the angles α and β will tend to zero, forcing all the atoms of the molecule into a common plane (into the mirror plane of the S_4 symmetry element in D_{2d}, represented by the dashed line). The phenomenon of molecular flattening under high pressure has been observed in other organic materials via vibrational spectroscopy, justifying the technique of choice [29].

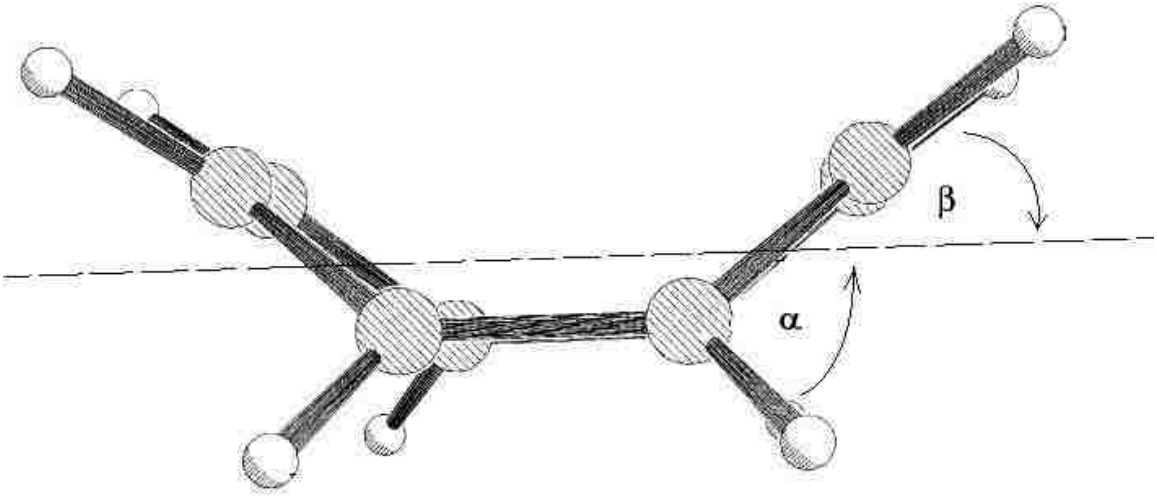

Figure 3. *Illustration of the COT molecule "flattening" into a planar conformation. Modified from [2].*

A natural question to follow the hypothesis of flattening under pressure is whether such a structural change at the molecular level would be accompanied by electronic changes that may lead to the resonant aromatic structure, characterized by a planar form with equal bond distances along the COT ring where the extra electron from the double carbon bond (from the nonplanar tub-structure) is delocalized to the entire ring. Hence it is hypothesized by this thesis that such a transformation/flattening from a nonplanar to a planar molecular structure might impose this equalization of bond distances along the ring, as one may speculate a causation from molecular planarization to aromaticity. The hypothesized transformation would then be from a nonplanar tub-shaped D_{2d} molecular structure to a planar form with a D_{8h} point group character possessing an 8-fold rotation axis perpendicular to the molecular plane. This structure of COT is considered in some studies as either a transition state [3,4,5], an anion [6], a dianion [7], or as an annulated molecule [8]. This of course violates Hückel's (4n+2) π-electron rule, since COT has 8 π

electrons, which would actually classify it as an unstable antiaromatic molecule if it were to become planar. Nevertheless, this work aims to resolve if such a pheomenon takes effect.

Considerations of aromaticity facilitates a comparison with its archetypical model, benzene. The benzene molecule is a single-ringed hydrocarbon that possesses an aromatic equilibrium structure, which provides the motivation to use it as an analogue to COT under pressure, for which aromaticity is being considered. Furthermore, a high-pressure comparison to benzene is facilitated due to the its relative pervasiveness and availability in high-pressure literature [9,10,11].

Hence, this study also serves as a possible contribution to the literature, as hydrocarbons in general are not extensively studied at high pressures. A Raman study of COT to 16 GPa has already been previously published [12], and this work is intended to complement it.

High-Pressure Spectroscopy

Measurement of Pressure: Ruby

Ruby is the common name for α-Al_2O_3:Cr, or Chromium-doped Corundum (α-Al_2O_3), the thermodynamically stable form of Aluminum oxide (Al_2O_3) at ambient conditions. It exhibits useful properties for high static pressure studies inside a diamond anvil cell (DAC), the most useful being its R1 flourescence line at 694.2 nm. This line shifts approximately linearly up to ~20 GPa, at a rate of 2.746 GPa per nanometer wavelength shift[4]. The rate is a result of calibration against the “known” NaCl 300 K isotherm [13].

Under ambient conditions, the R1 line is part of a doublet (with R2 at 692.8 nm), a splitting of the ^2E level upon introduction of a trigonal crystal field, via the crystal structure of ruby. The ^2E levels are populated by non-radiative decay from the Y and U energy bands, which are in turn usually populated by laser pumping (See Figure 3) [14].

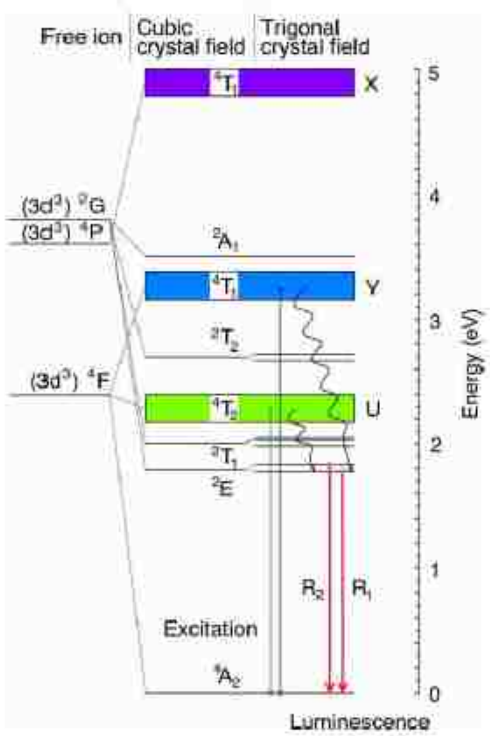

Figure 4. *Ruby luminescence energy level diagram (taken from [14]).*

<u>Vibrational Spectroscopy</u>

Vibrational spectroscopy probes the quantum transitions between vibrational states. To first approximation, the molecular potential well is conventionally modeled by the harmonic (parabolic) potential $U(x)=Cx^2$, where C is the spring constant from Hooke's law, which when applied to Schrodinger's equation yields the expression for allowed

quantized energies E between successive vibrational states: $E = (v + ½) h\omega_0$ where v is the vibrational quantum number and where $v \geq 0$ and is an integer. Here h is Planck's constant and ω_0 can be equated to the classical vibrational frequency:

$$\omega_0 = \frac{1}{2\pi}\sqrt{\frac{C}{\mu}}$$

where C is the force constant and μ is the reduced mass. The value of C is determined by the intramolecular forces in the molecule, and μ is determined by the masses involved in the particular vibration. To excite these vibrations a quantum of energy E must be absorbed by the system, promoting the molecule to the next higher vibrational state. A subsequent de-excitation of the system to the lower state expels an energy quantum $E = h\nu$ in the form of a photon (where ν is the photon frequency). The selection rule $\Delta v = \pm 1$ for a parabolic well limits the transitions to adjacent energy levels.

This is the process inherent to a vibrational spectroscopy experiment. In an infrared experiment, photons with frequencies that correspond to vibrational energies are absorbed and re-emitted toward a random direction in space that goes unregistered by a fixed detector. In a Raman experiment the same photon is absorbed, re-emitted and collected by a fixed detector. Infrared spectroscopy records all of the photons absorbed, whereas Raman spectroscopy records a fraction of the photons emitted – accounting at least in part for Raman's much weaker effect.

The harmonic potential well, as stated, is an idealization of real molecular potential wells are never truly parabolic. Nevertheless, the equation serves as a good approximation near the equilibrium positions of the atomic constituents of a molecule.

Further from the equilibrium position, however, the harmonic potential approximation becomes more tenuous, and an anharmonic term to the molecular potential must be included [15]. Consequently, the fundamental transitions are not equally-spaced; the energy gaps decrease with increasing energy. Another consequence of the anharmonicity is the weak probability of "forbidden" transitions. One such type are called overtone transitions, where the excitations/de-excitations by a single photon are to non-adjacent vibrational levels (i.e. $\Delta\nu \neq \pm 1$). Combination bands are also allowed, in which multiple vibrations are excited by a single photon. Within the combination band classification are difference and sum bands. A difference band is that of a simultaneous excitation of a vibrational mode and de-excitation of another. An example is a system with two normal modes <a| <b| making a <0|<1|→<1|<0| transition, where the transition energies are E_a and E_b. The observed frequency will then be $\upsilon = |E_a - E_b|/h$; the jettisoned photon is imparted with the difference between the two transition energies. Likewise, a sum band consists of two or more simultaneous excitations of fundamental vibrations. The observed frequency is the sum of individual transition frequencies (minus the small anharmonic contribution). Fermi resonance is also a possibility, in which two or more vibrational modes of the same symmetry species may cross each other (forbidden under the harmonic approximation). This usually results in the exchange of peak characteristics such as intensity and width [16]. For most of our work, we are concerned with the $\nu=0$ to $\nu=1$ fundamental transitions.

Raman Spectroscopy

One way the vibrational transitions of a molecule can be sampled is via Raman spectroscopy, in which the incident photon couples to the molecule's electric polarizability. The electric polarizability α is defined by the relationship between the induced dipole moment and the electric field strength:

$$\boldsymbol{p}_{ind} = \vec{\vec{\alpha}}\boldsymbol{E}$$

in which α is a 2nd rank tensor. The induced dipole is caused directly by the field, as the presence of an electric field separates the positively charged nuclei and negatively charged electrons. The Raman effect is derived classically from a non-constant value for α, or otherwise a space-varying polarizability α(q), where q represents the vibrational displacement. To a first order approximation, α(q) is linear with q about the equilibrium polarizability α_0 [17]:

$$\alpha = \alpha_0 + \left(\frac{\partial \alpha}{\partial q}\right)_0 q$$

A time-varying 1-dimensional electric field gives:

$$\varepsilon = \varepsilon_m \cos(2\pi \nu t)$$

and a molecule will vibrating at its natural frequency ω gives :

$$q = q_0 \cos(2\pi \omega t)$$

Inserting all the Eqs. into the definition of α, we get:

$$\begin{aligned} p_{ind} &= \alpha \varepsilon \\ &= \left(\alpha_0 + \left(\frac{\partial \alpha}{\partial q}\right)_0 q\right)(\varepsilon_m \cos(2\pi \nu t)) \\ &= \alpha_0 \varepsilon_m \cos(2\pi \nu t) + \left(\frac{\partial \alpha}{\partial q}\right)_0 q \varepsilon_m \cos(2\pi \nu t)\cos(2\pi \omega t) \end{aligned}$$

Using the trigonometric identity $\cos(a)\cos(b) = \frac{1}{2}(\cos(a+b) + \cos(a-b))$, we get that:

$$p_{ind} = \alpha_0 \varepsilon_m \cos(2\pi\nu t) + \frac{1}{2}\left(\frac{\partial\alpha}{\partial q}\right)_0 q\varepsilon\left[\cos(2\pi\{\nu+\omega\}t) + \cos(2\pi\{\nu-\omega\}t)\right]$$

This last equation shows that the induced dipole moment p_{ind} will oscillate (and hence scatter) at frequencies of υ (Rayleigh scattering), υ+ω (anti-Stokes radiation), and υ-ω (Stokes radiation). The Stokes and anti-Stokes radiation account for the Raman effect, and they will be observed as frequency shifts from the Rayleigh line.

These shifts can be sampled by a dispersive spectrometer, which takes in the scattered light and disperses the light intensity as a function of frequency via a grating into a strip detector. The Raman frequency shifts will then appear as vibrational peaks in the intensity vs. frequency spectrum. The incident, monochromatic Rayleigh line is usually provided by a laser, of much higher frequency than the Raman shifts, as the scattering efficiency scales with the lasing frequency.

Infrared Spectroscopy

The interaction of the electromagnetic field with a molecular vibration is dominated by the electric field; the magnetic field contribution is negligible. This coupling is mediated by the molecule's electric dipole moment $\boldsymbol{p}$, which is defined by the classical definition $\boldsymbol{p} = q\boldsymbol{d}$, desciribing a system of two charges $+q$ and $-q$ separated by a displacement vector $\boldsymbol{d}$. Hence a molecular vibration that is symmetric about the bond will not produce a net change in $\boldsymbol{p}$ and will not be IR-active.

The fact that it is a material's electric dipole moment that couples directly to the field

makes sense in that a charge separation would feel the effect of an E-field. A range of photon frequencies in the IR region in particular are used for the incident beam since the typical energy gaps of vibrational transitions are in the IR range in accordance to $E=h\upsilon_{photon}=h\omega_{vibration}$. Hence in IR spectroscopy, a broadband source of IR light (in contrast to Raman which uses a monochromatic source) impinges on a sample which absorbs photons that match the vibrational energy gaps. The absorbed photons then appear on the detector as "missing" bands in the spectrum, or absorption peaks. The electric field-dipole coupling that is the mechanism for IR spectroscopy makes sense from the perspective of a classical resonance phenomenon where the oscillating electric field drives the frequency-matched molecular vibration[16].

FT-IR

Fourier-Transform Infrared (FT-IR) spectroscopy is a technique utilized to acquire the IR spectrum of a material more efficiently than a dispersive spectrometer. This uses both the power of the Fourier transform and the Michelson interferometer to capture a wide range of frequencies in one acquisition. The Fourier Transform is given by a pair of related equations:

$$f(x) = \int_{-\infty}^{\infty} F(\tilde{\nu}) e^{\iota 2\pi \tilde{\nu} x} d\tilde{\nu} \equiv \widetilde{F}(\tilde{\nu})$$

$$F(\tilde{\nu}) = \int_{-\infty}^{\infty} f(x) e^{-\iota 2\pi \tilde{\nu} x} dx \equiv \widetilde{f}(x)$$

where the identities denote that the $f(x)$ is the Fourier transform of $F(\tilde{\nu})$, and vice-versa.

As with convention, the symbol x represents the spatial dimension and $\tilde{\nu}$ represents the wavenumber (and is the inverse of wavelength $\tilde{\nu}=1/\lambda$). The wavenumber represents the frequency domain ν , and are related through $\nu=c\tilde{\nu}$ where c is the speed of light. So essentially, the Fourier transform allows for switching between the space and frequency dimensions. This is the operation that is in effect in an FT-IR instrument, as the raw data is recorded in the form of an interferogram (in x space) which has to be "back"-transformed into frequency space, to finally show the component vibrational modes in the molecule under study. Recording in x-space is what enables the multiplex advantage of the technique – being able to capture a wide range of frequencies simultaneously. The range of frequencies is of course limited by the range of the interferogram's travel, which will be described later.

The finite limits on a real interferogram brings forth two obvious issues; the functions in the Fourier transform are continuous and the transform itself is defined with infinite limits. To make the transform applicable to an actual experiment (where data is finite), the functions $f(x)$ and $F(\tilde{\nu})$ must be discretely sampled and the limits of the mathematical transform truncated to satisfactory limits.

This is done through the Discrete Fourier Transform (DFT), which is given by:

$$F(\tilde{\nu}_k)=\frac{1}{N}\sum_{j=1}^{N} F(x_j)\mathrm{e}^{-\iota 2\pi x_j \tilde{\nu}_k}$$

where

$$x_j=(j-1)\delta x \; for \; j=1,2,3,\ldots$$
$$\tilde{\nu}_k=(k-1)\delta\tilde{\nu} \; for \; k=1,2,3,\ldots$$

where x_j is the jth data point in x -space, and $\tilde{\nu}_k$ is the kth data point in $\tilde{\nu}$ -space. δx

and $\delta\tilde{\nu}$ are the distances between data (sampling) points in the x - and $\tilde{\nu}$ - spaces, respectively. N is the number of sampling points [28].

The DFT is the implementation of the Fourier Transform in real-world instrumentation, where a mathematical continuum of data is not realizable. Although, it is the software that takes the discrete function $F(x_j)$ collected by the interferogram and inserts it into the DFT to produce another discretized function in frequency space, $F(\tilde{\nu}_k)$. $F(x_j)$ gives the interferogram and $F(\tilde{\nu}_k)$ gives the spectrum. The actual algorithm that optimizes the DFT is called the Fast-Fourier Transform, which cuts down the computational load of the process, but a description of which is beyond the scope of this work [18].

The Michelson Interferometer

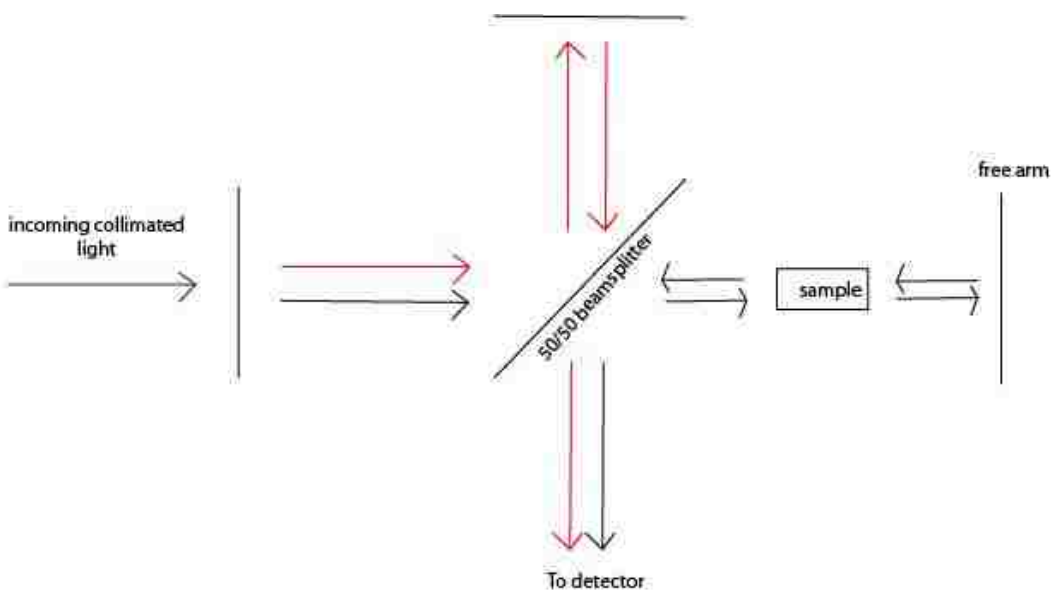

Figure 5. *Diagram of a Michelson interferometer.*

The Michelson interferometer is illustrated in Figure 5. The interferometer in its essence consists of two mirrors and a half-silvered beamsplitter (ideally 50% transmitting and 50% reflecting). One mirror is fixed in place and the other (known as the interferometer arm) is free to linearly translate orthogonal to its plane. The incoming beam is collimated so that the light traversing the interferometer consists of plane waves and has minimal divergence. The output is then refocused onto the detector.

The interferometer separates an incoming beam of light into a transmitted and a reflected component at the beamsplitter. The two paths are shown in Figure 5, the transmitted (red) path is the reference beam and the reflected (black) path carries the absorption information with it. The starting/zero position is marked by where the two beams paths have a zero retardation Δ or optical path length (OPL) difference . Hence at this position, $\Delta = |OPL_1 - OPL_2| = 0$. When the two beams are then joined at the beamsplitter, the electric fields from the separate beams interfere and the wave sum is collected by the detector. As the moveable arm is swept through its limits, the combined signal is discretely sampled at equally-spaced time intervals and the recorded intensity I(x) as a function of the free arm's travel distance x (from Δ=0) produces the interferogram.

A perfectly monochromatic source with no material sample along the “black” path will display an interferogram I(x) that is perfectly cosinusoidal (symmetric about the zero position), in agreement with the Fourier transform of a delta function into a cosine wave. A continuous polychromatic source that is some general function of frequency will exhibit a more complex profile, as individual cosine waves of each frequency in the

spectrum are superimposed to make the interferogram. In general, the interferogram's main features will show a maximum intensity at $\Delta=0$, exponentially decaying as x increases. For vibrational spectroscopy, an FT-IR is utilized with the material sample in the path of the "black" beam, where the frequencies in the source spectrum that correspond to vibrational modes present in the sample are absorbed. Those absorbed frequencies are observed as peaks in the absorption spectrum [18].

Detectors

Detectors for IR spectroscopy as classified with respect to their detection mechanisms into two main groups: thermal detectors and photon/quantum detectors. Thermal detectors function by measuring a change in a temperature-dependent physical property of some material such as electrical resistance (bolometer) or electric polarization (pyroelectric detector). This change is caused by the absorption of electromagnetic radiation which carry with it energy that thermally agitates the detector material, hence changing its temperature. On the other hand, the photon detector uses the quantum transitions in the detector material to detect a change. In a semiconducting material, incident photons excite valence band electrons into the conduction band (leaving holes behind), causing a spike in the current carriers available and hence an increase in current output. Mercury Cadmium Telluride (MCT) detectors fall into this type of IR detector [19].

For Raman experiments, the use of a charge-coupled device (CCD) detector is common, which is essentially a photoelectric material detector fixed on an array of

capacitors, where a capacitor fixed on a particular pixel collects charge expelled by a corresponding strip of photoelectric material during a data acquisition; the intensity of the light is then proportional to the amount of charge collected. The bank of charges are then moved pixel by adjacent pixel to an integration circuit to reconstruct and process the image. The active area of the CCD is binned so that it functions as a strip detector suitable for spectroscopic measurements.

Synchrotron Radiation

Synchrotron Radiation (SR) is the emission of electromagnetic radiation from charged particles (usually electrons or positrons) traveling near the speed of light. Facilities dedicated to their production (synchrotron storage "ring" facilities) are used to extract a high-brightness beam for general use, one of which is infrared spectroscopy. The spatial profile of this relativistic emission is a tangentially-directed cone of light released orthogonal to the acceleration vector, but coplanar with it and the velocity vector. Hence a charged particle traveling in a circular ring will release a conical jet of radiation concentrated in a small solid angle at tangent lines to that circular path in the direction of the velocity vector, which lends to its use as a beam source. This is contrary to an nonrelativistically accelerating charged particle, which will emit light with a dipole spatial profile.

The charged particles are guided into the closed-loop path (called the storage "ring") by a series of magnets. The energy lost in orbit through radiative emission (synchrotron radiation) is replenished by radio frequency (RF) cavities along the track, which are

essentially chambers in which an oscillating electric field persists in the RF range. This oscillating electric field carries with it the orbiting charges, which develop into a “bunch”, or a localized grouping of the charges. The width of the bunch is determined predominantly by the cavity frequency and circumference of the ring facility. As a consequence of the bunching, the synchrotron radiation output is pulsed. The extraction points of the radiation are, as in the theory, where the charges are accelerated. In the case of a perfect circle, the facility would output synchrotron radiation at all points of the path [20].

However, many facilities are not constructed as perfect circles, but as straight line segments joined at curved vertices, where the acceleration and radiation emission occurs. This is the case with the NSLS VUV (Vacuum-Ultraviolet) storage ring which was utilized for the experiment, where radiation emitted from one of the ring's eight vertices is extracted by a bending magnet port (U2) at that vertex. Normal operations for the VUV storage ring include a fill current of 850 mA at a beam energy of 808 MeV. The U2 port delivers beam dimensions of 40 x 80 mrad, which is divided into two beams, one of which is directed to the U2A user facility or “hutch”, housing the FT-IR spectrometer used for the experiment. Between the bending magnet and the U2A hutch, an optical system composed of ellipsoidal and planar mirrors as well as diamond and KBr windows filter and collimate the beam before it enters the spectrometer [21].

CHAPTER 2

EXPERIMENTAL PROCEDURES

High-Pressure Generation

For an experiment, a diamond anvil cell (DAC) housing an matched pair of diamonds were glued to stainless steel seats. For the mid-infrared (MidIR) experiment, a Princeton-design symmetric cell was utilized. For the far-infrared (FarIR) experiment, a Japanese-design (Syntek) DAC was used. The Raman experiment used a 3-pinned Merrill-Bassett cell. The following procedures are referenced to the symmetric cell but are in essence the same procedure for the 3-pinned cell.

Figure 6. *A Merrill-Basset 3-pinned DAC was used for the Raman measurements.*

Figure 7. *Symmetric type cell was used for the IR measurements.*

[Photo Courtesy: cars9.uchicago.edu/gsecars/photos7.jpg]

Figure 8. *Diamond mounting jig.*

Figure 9. *Electronic Discharge Machine (EDM).*

A DAC essentially consists of two opposing diamonds with their tips (culets) contacting. The small area of the culets provide the means for generating high static pressures through moderate applied loads, supplied by screws on the body of the DAC. This screw actuation pushes the diamonds toward each other, transferring the load to the culet tips. The diamonds sit on tungsten carbide "seats", which act as supports for the applied load. The preparation of a DAC is as follows:

Both seats are fixed on opposing halves (one called the piston, the other the cylinder) forming the DAC. The components for both piston and cylinder are first assembled, and then the two halves are aligned relative to each other. The critical property during the assembly procedure is the alignment of the overall DAC system, which heavily influences the success of the experiment by maximizing the terminal pressure to higher regimes. The terminal (maximum) pressure of the experiment is dependent on many

factors, such as gasket hole stability, hardness of medium, DAC construction and type; but proper centering serves to keep this limit as high as possible, all other variables being the same. All alignment is aided by the use of a monocular microscope to enhance tolerances. Care is taken to guarantee the best possible parallelism of the two culet surfaces by cleaning all mechanically contacting surfaces (interfaces).

To prepare a DAC, we first mate the diamond table/seat interface. The diamond is centered on the seat with the use of a mounting jig (Figure 8). The jig supplies a normal force orthogonal to the interface/table plane (z-direction) to keep the diamond in contact with the seat, and is fitted with 4 actuator set screws in the plane of the table seat interface (x-y plane), allowing for the X-Y alignment of the seat relative to the culet. Once optimal microscopic alignment has been determined, the diamond is glued to the seat via an epoxid resin, fixing the diamond to the seat.

Once the diamond and seat are glued together, the seat is then interfaced with the cell half-body. A similar X-Y alignment system consisting of 4 set screws (3 on a Merrill-Basset DAC) on the half-body is used, aligning the seat to the body. Once this operation is completed for both piston and cylinder, the two halves are brought together gently, just close enough to have a thin gap of air in between the diamonds. The diamonds are then viewed along the symmetric (z) axis of the cell under the microscope, and the perimeter outlines of the two diamond faces are aligned to the best possible tolerance, using the set screw system. The entire procedure allows for the best possible alignment between successively smaller components (from half-body to seat to diamond), allowing for the best transfer of load applied from the screws.

A gasket is then prepared by punching a stainless steel sheet from shim stock of about 0.01 inches (250 microns) with a round flat punch, fabricating a gasket diameter of about ¼ inch. The gasket is then flattened under a vice to even out the thickness, and then also deburred and lapped using sandpaper. The gasket is then cleaned and fixed onto the cylinder half-body, resting against the diamond's culet supported by clay adhesives around the contacting surfaces. The two DAC halves are then gently assembled together with the load screws, and a small load is applied to create a thin indentation in the gasket. Indenting the gasket hardens the thinned area of the material between the diamonds and allows for a higher terminal pressure. The gasket is recursively removed and the indentation depth checked with a micro-caliper until the desired gasket thickness is reached.

A hole is drilled in the center of the gasket to a specified diameter via electron ablation using an Electrical Discharge Machine (Figure 9). An EDM consists of a conducting wire translating in the z-direction towards an electrical plate, with an applied voltage between the wire and the plate. As the wire nears the plate, an electric field between the two exceeds that of the dialectic breakdown of the medium in between the plates, and an electrical arc is generated. It is this projected current that erodes the plate or whatever material is placed on top of the plate, in this case the gasket. The gasket is then removed from the DAC and put into the EDM platform, and centered with respect to the drilling wire of a specified wire guage to match the desired hole diameter. This step ensures that the hole is maximally centered on the indentation. A stage with X, Y, and rotational actuators along with a fitted microscope is used to facilitate this alignment

process. Once aligned, fluid such as mineral oil or isopropanol is introduced into the stage cup to serve as the dielectric, allowing the tip to get closer for precision drilling. The drill is then activated and the position monitored with a voltmeter that converts the relative placement of the drill tip to a voltage reading. Once the drill breaks through the entire gasket depth, the drill's rate of travel (and thus the voltmeter reading) spikes, signaling that it has drilled through the entire material. The gasket is then ultrasonically cleaned and reinstalled on the diamond anvil. The volume drilled out from the hole at the center of the gasket forms the sample chamber, sealed by the walls of the opposing diamond culets. This will contain the sample under study and will be the target for the applied load.

In summary, Table 1 lists the various experimental geometries used in the 3 experiments.

Table 1.*Experimental parameters for the 3 separate loadings/measurements.*

	culet diameter (μm)	gasket hole diameter (μm)	initial gasket thickness (μm)
MidIR	300	130	20
FarIR	300	110	50
Raman	500	120	80

Infrared Experiment

The available setup at the U2A beamline is given by the Figure 10. The synchrotron beam is redirected from the U2 port and terminated as a collimated infrared beam

incident on the sample under load. There are separate detectors for the MidIR and FarIR placed at two different locations on the rig; an MCT detector is used for the MidIR range while a bolometer is used for the FarIR. Two separate experiments were conducted for each frequency range, about one year apart. There is also a ruby/Raman spectrometer setup adjacent, and the DAC is moved between the IR and ruby setups for each pressure, to take a spectral acquisition and measure pressure recursively. The ruby spectrum was taken before and after every IR measurement, to yield the range in pressure that the sample experiences in the short time that vibrational data was taken. This is to account for any relaxation of the gasket over time, which is known to happen [22].

On the table is a Bruker 66v/S vacuum FTIR, with a frequency range of 10-10000 cm^{-1} and a maximum resolution of 1 cm^{-1}. The data acquisition is controlled by the OPUS NT v4.0 software. For Mid-IR measurements a Bruker IRscope II was utilized, with a frequency range of 600-100000 cm-1, as limited by the mid-range MCT-A detector. The actual range of data for the MidIR experiment spanned from 600-5000 cm^{-1}, beyond which no prominent spectral features were observed. For Far-IR measurements, a custom optical setup was utilized with a working distance of 40mm. The Far-IR experiment ranged from 100-700 cm^{-1}. Both MidIR and FarIR measurements yielded a resolution of 1.92 cm^{-1}. The visible spectrometer/fluorimeter setup used for the ruby measurements provided a measurable spectral range of 400nm – 1.06 microns, with a maximum resolution of 0.03 nm.

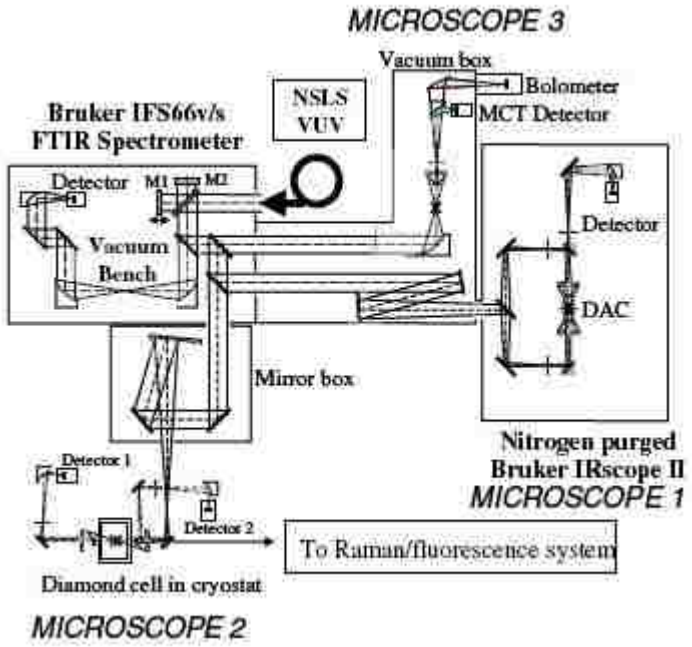

Figure 10. *Schematic of the U2A beamline setup [21]. Microscope 1 was used for the MidIR experiments and Microscope 3 for the FarIR.*

The DAC is adapted to the FT-IR setup at the U2A beamline at the National Synchrotron Light Source (NSLS) at Brookhaven National Labortatory. For the MidIR experiment, the aperture of the incident beam was limited to a ~50 x 50 μm^2 area, and for the FarIR experiment the aperture was opened to the diameter of the gasket hole to prevent diffraction. A background spectrum in both cases was also taken by placing the DAC without the sample in the setup, in order to best approximate a spectrum of the sample itself. The result, after subtraction and transformation, is the absorbance spectrum:

$$I_{sample,\,absorbance} = -\log\left(\frac{I_{raw,\,transmission}}{I_{background}}\right)$$

This of course neglects the small reflective term. Transmission data was collected for

the experiment, and was converted into absorbance data automatically using the above expression. The DAC was taken apart to allow two annealed ruby spheres to be added into sample chamber (the hole in the gasket) to serve as pressure measurement probes. The liquid sample of 1,3,5,7-cyclooctatetraene (with 0.1% hydroquinone added for stabilization) was then also loaded into the sample chamber via a sanitized syringe, and then sealed by the two opposing diamond anvils.

A series of IR measurements were then performed on the sample volume. The raw signal amplitude was checked periodically to ensure that a primary beam passed through the sample. Incremental steps in pressures were taken; the pressure is measured both before and after the IR spectrum is measured using an adjacent laser/spectrometer setup dedicated to high-pressure ruby flourimetry.

The level of the spectrum was adjusted to avoid saturation of the detector by thinning the gasket sufficiently, decreasing the maximum intensity of the peaks as a result. Multiple spectra were averaged to produce the recorded spectrum for each pressure point, utilizing the multiplex advantage of an FT-IR spectrometer over a dispersive instrument, creating a low noise spectrum. Moreover, measuring the vibrational spectrum via an infrared beam circumvents the prominent fluorescence curve contributing to the background of the COT Raman spectrum, as its yellow-green color at ambient conditions would indicate. The experiment was terminated due to a limit on the allocated beamtime at NSLS, to a sample terminal pressure of ~25 GPa but with spectral data of only up to ~20 GPa .

Raman Experiment

For the Raman experiment, data for three spectral regions were acquired by using a micro-Raman dispersive grating spectrometer setup (Jobin-Yvon Triax 550). A schematic is provided in Figure 11. The 647.1 nm excitation of a Krypton-ion (Lexel RamanIon) continuous-wave laser was used to illuminate the sample with the Rayleigh line around which the Raman shifts may be observed. The apparatus allowed for a resolution of about 3.5 cm^{-1}. The sample was loaded in a Merrill-Bassett type cell due to a working space limitation, since the cell is much shorter than the symmetric-type DAC.

First the grating was set to center around a certain wavelength and thus determine the range of spectral data for the acquisition. Then the spectrometer was calibrated with a gas spectral emission lamp, where the "known" spectral peaks appearing around that wavelength are manually picked out with the computer cursor and set to define the wavenumber (Raman shift) axis.

The setup focused the beam on the order of 5 mW into a ~10 μm diameter spot on the sample and away from the small ruby sphere and thus its strong fluorescence. This is done via visual inspection (with the aid of laser safety goggles tuned to the laser light frequency) with a confocal microscope. Then a beamsplitter is moved into the path of the beam to redirect it from the microscope eyepiece to the spectrometer. The pressure is measured by centering the beam spot near the ruby and moving/calibrating the grating to around the ruby wavelength.

The range of wavenumbers accessible to a single measurement did not span the entire range of interest, so the monochromator was moved to three different regions for every

pressure point (centering the grating around 668nm, 690nm, and 725nm). The spectrometer/grating was calibrated after each time it was moved.

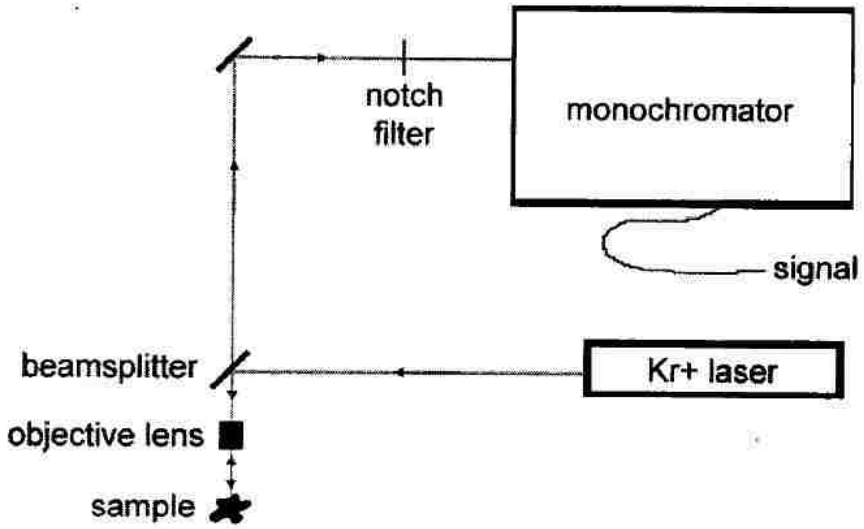

Figure 11. *Schematic of the micro-Raman setup. [23]*

CHAPTER 3

RESULTS

The main set of results gathered from these studies is the evolution of the spectral peaks over pressure. Hence the graphs of interest are of peak positions as a function of pressure measured inside the DAC. A brief description of how these x and y values were attained is appropriately given in the following sections.

The Pressure(X) Axis

For all the experiments, the ruby fluorescence spectra were fitted to Lorentzian peak profiles. Pressure is then determined from the fitted peak position of the R1 ruby through the accepted linear calibration of the ruby scale: $P(GPa)=2.746(\lambda-\lambda_0)$ where λ_0 is the R1 peak position at ambient pressure (~0 GPa). This carries with it a calibration error of roughly 5% [14]. The reported value for the average pressure of the sample is determined by averaging the fitted peak positions of the two pressure measurements taken before and after an IR spectral acquisition.

The λ_0 values used for the separate experiments are λ_0=694.337 nm for the FarIR and Raman experiments and λ_0=694.32 nm for the MidIR. These values were extracted from zero-pressure fluorescence spectra of the batches of ruby spheres used in the different experiments. The λ_0 value for the FarIR and Raman experiments are the same since they both came from a common batch; the ruby sphere used in the MidIR experiment came from a separate batch. The rubies in a common batch are made from the same melt, and should give similar readings.

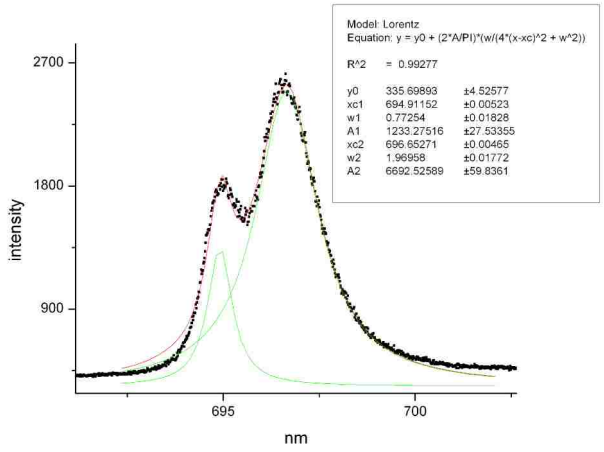

Figure 12. *A rough fit of the Ruby R1 and R2 peaks with Lorentzian profiles at P ~ 7 GPa.*

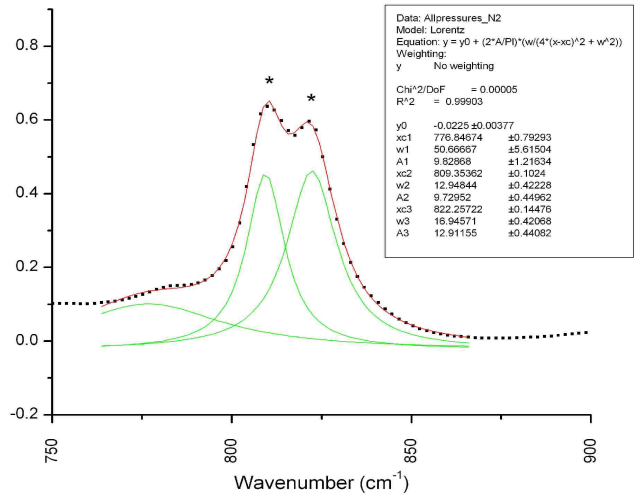

Figure 13. *An example of the locally fitted background. The leftmost unstarred peak is fitted to a Lorentzian to better extract the positions of the 2 overlapping (starred) vibrational modes.*

For the MidIR experiment, the R1 fits give visually adequate results but do not exactly model the ruby spectrum's lineshape (Figure 12), and so the error of the fit does not properly describe the uncertainty in the peak position, and hence pressure. Moreover, a significant unquantifiable systematic error is suspect. The steady increase in the Lorentzian fit widths over pressure indicates a smearing of the sample pressure (under hydrostatic conditions, the R1 line has been reported to actually slightly decrease) [14]. To this effect, the R1 width increases from ~1 nm at 1.5 GPa to be ~2 nm at 5 GPa.

Nonhydrostaticity sensed by the ruby sphere at its local environment translates to a larger gradient in pressure across the rest of the sample chamber. This pressure gradient could have potentially been quantified by placing ruby spheres across the chamber, since the R1 widths alone do not sufficiently correlate to a pressure gradient and hence cannot provide a quantitative measure [24]. Using a single ruby sphere allows for a quicker measurement during the finite allotted user time at U2A, but that advantage is severely offset by the lack of confidence in the pressure values. A likely compromise is to use two rubies (one near the center and another at the perimeter of the chamber), which was actually attempted but failed. Only one ruby was retained during the loading, as the other was washed out when the DAC was sealed. Consequently, no reliable error can be placed on the reported stresses. It must be noted that errors of the peak fit and ignore a substantial gradient across the sample; they do not truly reflect the uncertainty in pressure across the sample chamber.

The ruby fluorescence spectra collected for during the FarIR and Raman experiments show less of a pressure broadening. The FarIR experiment's R1 widths display an

increase from ~0.6 nm at 1 GPa to ~0.7 nm at 5 GPa. The Raman experiment's R1 width values, however, show no consistent upward trend and display a wide spread of fluctuation over pressure. As in the MidIR experiment only one ruby was successfully loaded in the FarIR and Raman experiments, giving the same problem with error determination. Likewise, no error is plotted on the Pressure (X) axes.

The Wavenumber (Y) Axis

The vibrational spectrum of COT reveals some significant changes over pressure, mostly observed in the splittings of certain intra-molecular modes, as well as the disappearance of others. The raw data is shown in stack plots for each of the individual experiments in Figs. 14- 18. The peak positions of these modes are tracked over pressure, also via a Lorentzian peak fitting procedure. Similarly, the choice of a Lorentzian lineshape is not based on any physical model but serves as a convenient choice that limits the number of free parameters experienced in the fitting procedures, since many peaks overlap in the COT vibrational spectrum. The least number of peaks were used to bring about a good representative fit of a spectral region with many overlapping modes to model the peaks under study. Whenever the background presents a prominent slope that would affect the peak position values, the background itself was locally fitted with a broad Lorentzian profile. The plotted (fit) error bars are typically quite small (within the size of the data points), but given that the fits were limited to regions where neither the entire background profile nor the peaks themselves were theoretically modeled, the reported fit errors are likely subject to a much larger systematic error. The fitting

procedure was executed mostly for consistency and reproducibility. An example is shown in Figure 13.

The MidIR data is given by Figure 14, the FarIR by Figure 15, and the three ranges of Raman data by Figures 16-18 [25]. Peaks of interest have been plotted in Figures 19-28. Some modes are correlated to their previously published zero-pressure assignments of intramolecular modes and is provided in Table 2 [26]. Hence, where zero-pressure data is displayed, it is taken from Ref. 26. Each mode with a found zero-pressure correlation is identified by a qualitative description of the symmetry coordinates involved in the normal vibration and its symmetry species in parenthesis. Note that the symmetry species assignment applies only to the free molecule at zero pressure. Most modes appearing in the Wavenumber vs. Pressure data do not have a zero-pressure correlate. However, the ones that do allow for some comment on what may be happening under pressure.

First, a comment should be made on the scatter of the Raman data. The beam width of the laser light impinging on the sample is very small compared to the sample area, and it can be expected that the local pressure measured by the ruby differs quite significantly from the local pressure of the sample where the Raman spectra were collected, which were not always at the same region in the sample chamber. Hence a lack of reproducibility in being able to place the laser spot at the same region can plausibly account for the fluctuation in the y-axis. Nonetheless, some qualitative conclusions can be drawn from the high-pressure behavior of the spectral modes.

Table 2: *Zero-pressure mode assignments as given by [26]. Observed values were used to correlate to high pressure data.*

Symmetry Species	C_8H_8		Approximate form of vibration
	Observed	Calculated	
	cm^{-1}		
A_1	3013	3016	C-H stretch (str.)
	1651	1662	C=C str.
	1221	1198	C-H in-plane (ip) bending (bend.)
	994	999	C-H out-of-plane (op) bend.
	873	873	C-C str.
	194	194	C-C=C bend.
A_2		3025	C-H str.
		1338	C-H ip bend.
		1184	C-H op bend.+C-C=C bend.
		793	C-C=C bend.+C-H op bend.
		301	Ring torsion
B_1	3013	3023	C-H str.
	1439	1442	C-H ip bend.+C-C str.
	994	997	C-H op bend.
	948	939	C-H op bend.+C-C str.
	655	661	Ring torsion+C-H op bend.
	249	247	C-C=C bend.+ring torsion
B_2	3015	3025	C-H str.
	1608	1615	C=C str.
	1204	1213	C-H ip bend.
	669	672	C-H op bend.
	285	288	C-C=C bend.
E	3015	3020	C-H str.
	2965	2986	C-H str.
	1640	1667	C=C str.
	1223	1222	C-H ip bend.
	1223	1149	C-H ip bend
	967	981	C-H op bend.+C-C str.
	942	924	C-H op bend.+C-C str.
	800	822	C-H op bend.+C-C str.
	625	606	C-C=C bend.+C-C str.
	365	362	Ring torsion

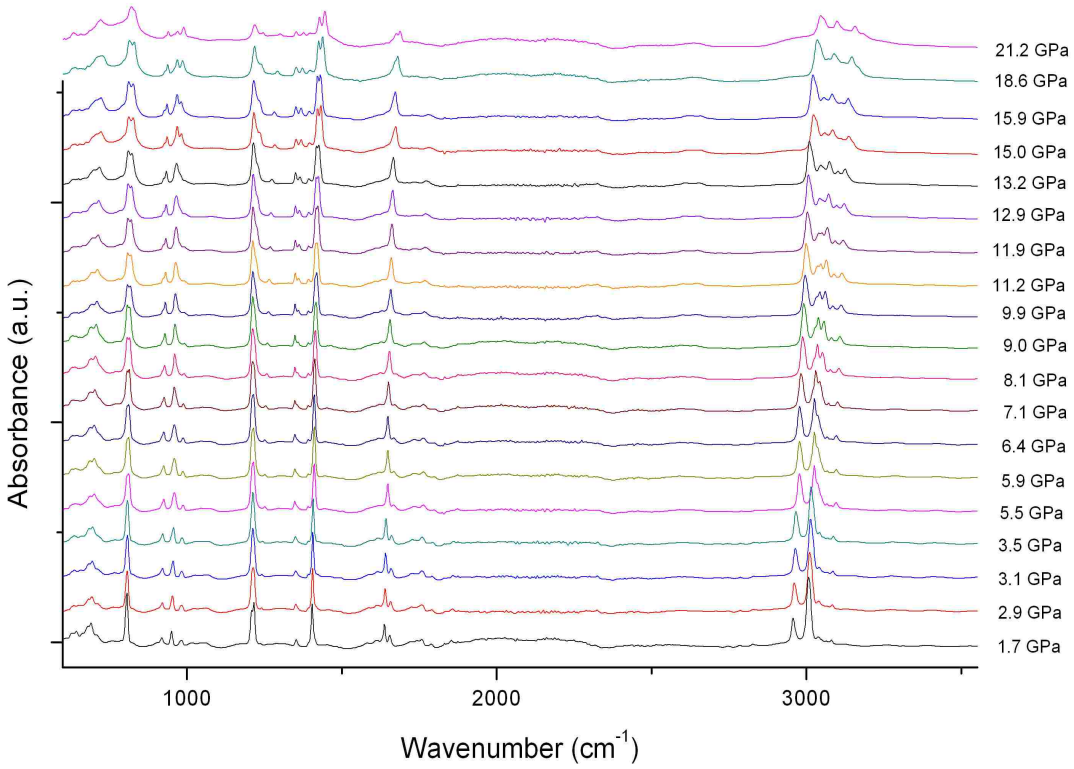

Figure 14. MidIR vibrational spectra raw data stackplot.

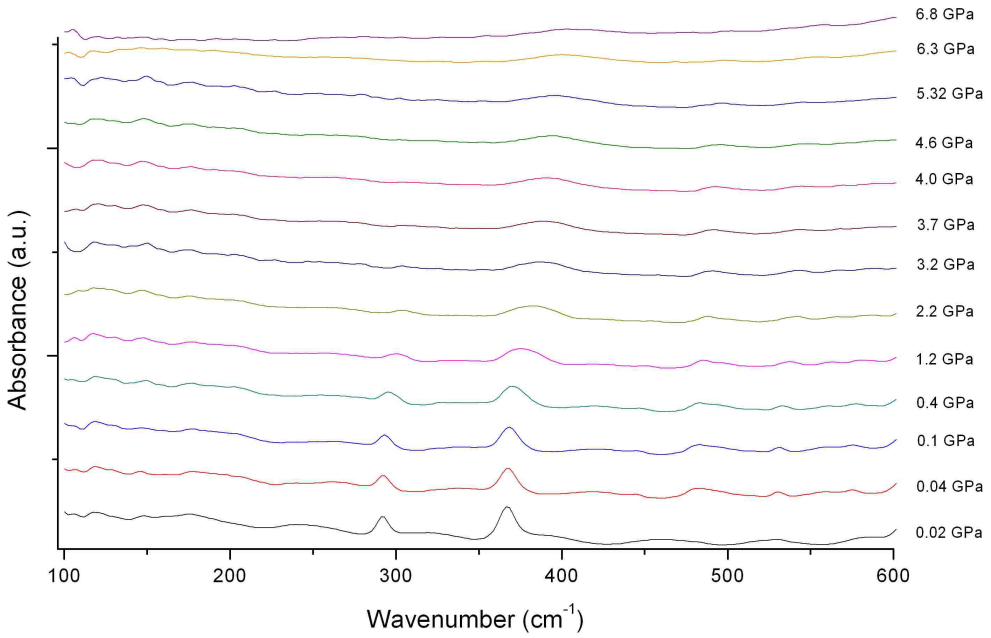

Figure 15. FarIR vibrational spectra raw data stackplot.

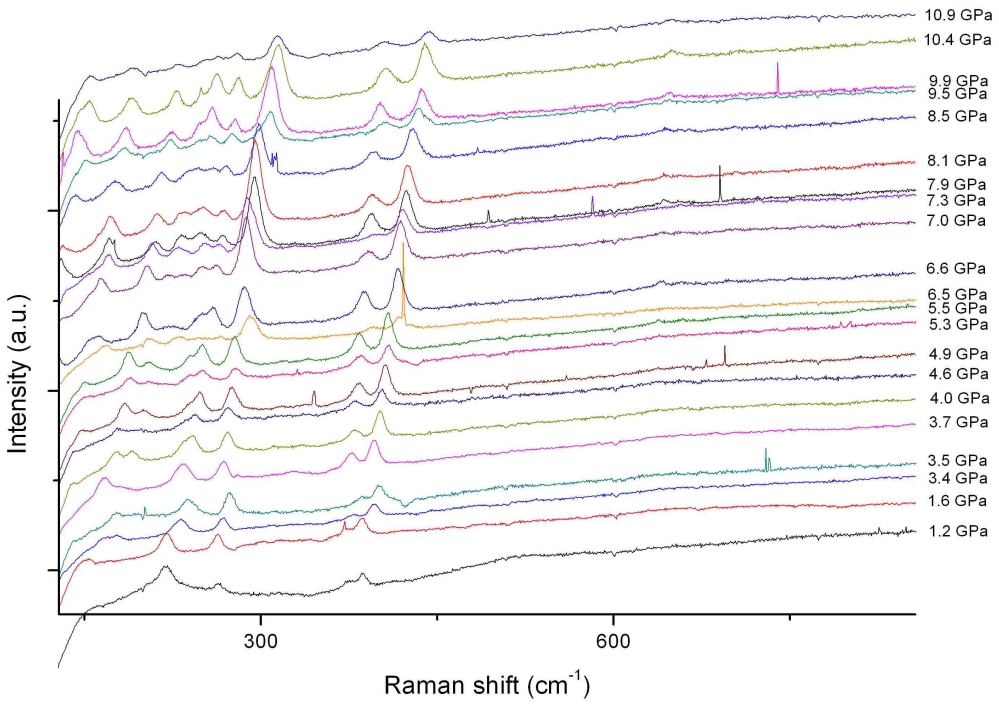

Figure 16. Raman vibrational spectra raw data stackplot 1. Grating centered around 668 nm.

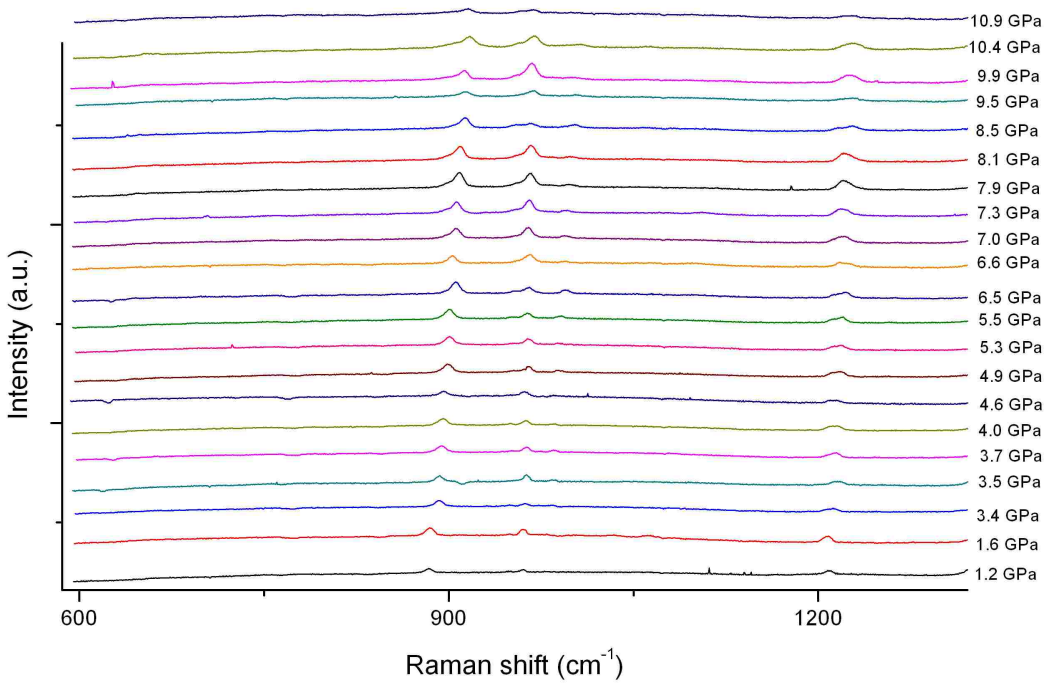

Figure 17. Raman vibrational spectra raw data stackplot 2.
Grating centered around 690 nm.

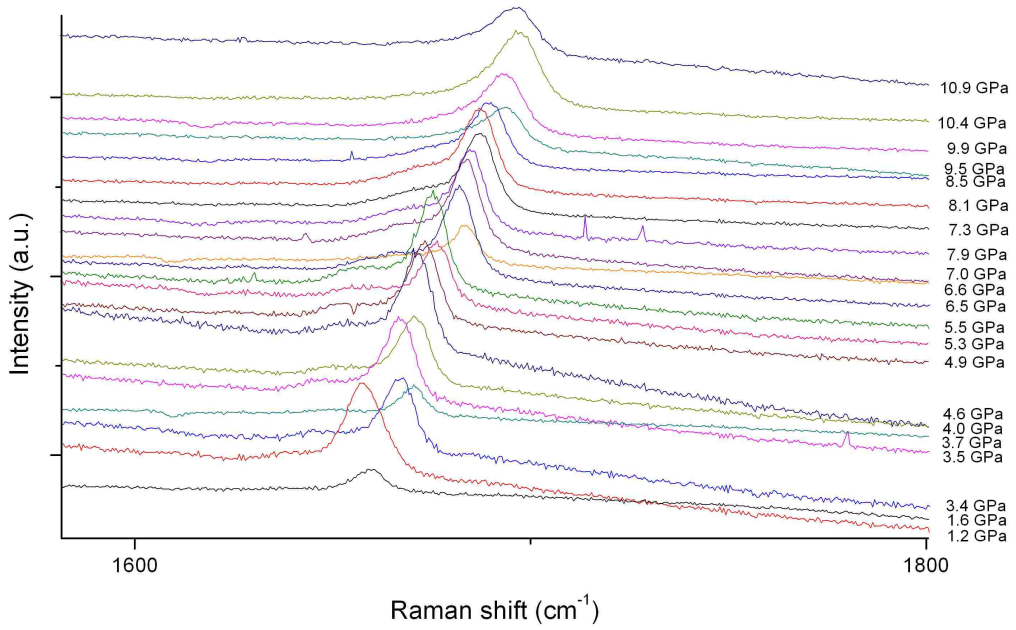

Figure 18. Raman vibrational spectra raw data stackplot 3.
Grating centered around 725 nm.

Discussion

Most of the vibrational modes follow the typical stiffening (blue-shifting) over increasing pressure. This makes sense in the context of the relation:

$$\omega_0 = \frac{1}{2\pi}\sqrt{\frac{C}{\mu}}$$

where the masses μ in the sample are invariant while the spring/force constants are increasing due to higher interatomic repulsions (due to the Coulomb force) that accompany an increase in pressure and density (and thus a decrease in interatomic distances). Some modes, however, exhibit more interesting behavior that allows for some analysis of what may be occuring to the molecule and the solid under high pressure. In particular, the data can reveal more on the hypotheses on flattening and aromaticity.

Flattening

The transition in the flattening of COT from a tub-shaped to a planar molecule would imply the decrease of the angles α and β in Figure 3. A likely result of this with regards to the vibrational spectra would be the "softening" of the C-H out-of-plane bending modes. The softening of a mode implies the red-shifting of the vibrational peak to lower wavenumber/energy/frequency over pressure. Such a red-shift would result from the weakening of the force constants involved in the vibration, as the equilibrium angle between the C-H bond and the COT ring decreases with higher pressures ($\alpha,\beta \rightarrow 0$ as the molecule flattens/planarizes). The pure C-H out-of-plane bending mode (B_2) in Figure 19 does not support this claim, as the mode consistently stiffens over pressure. Other fundamental vibrations that involve the C-H out-of-plane bending vibration are those shown in Figures 19 and 20 (in the IR data) and Figures 21 and 22 (in the Raman data)

through modes mixed with C-C stretching vibrations, but they do not show any trend of softening either.

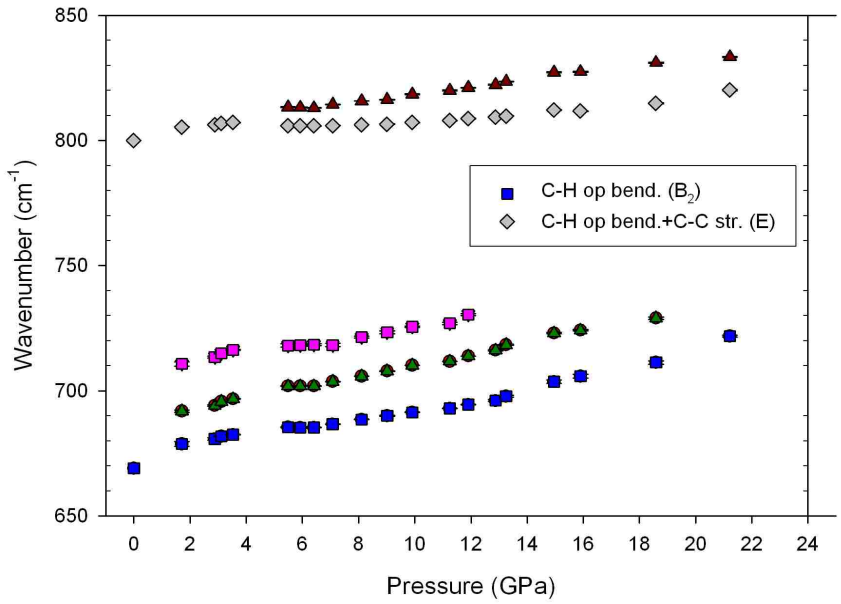

Figure 19. C-H op bending mode region (MidIR).

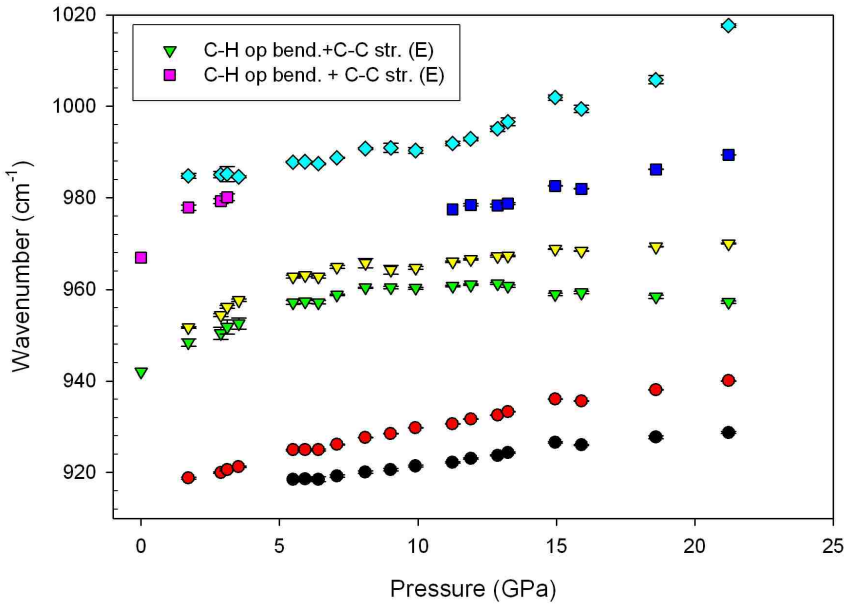

Figure 20. C-H op bending + C-C stretching mode region (MidIR).

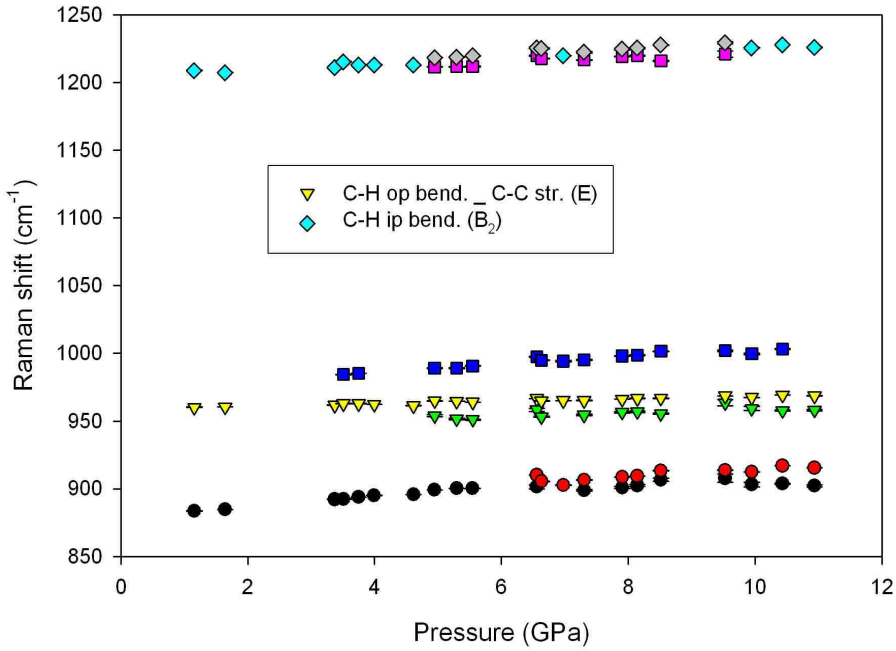

Figure 21. C-H ip bending mode; C-H op bend + C-C stretch (MidIR)

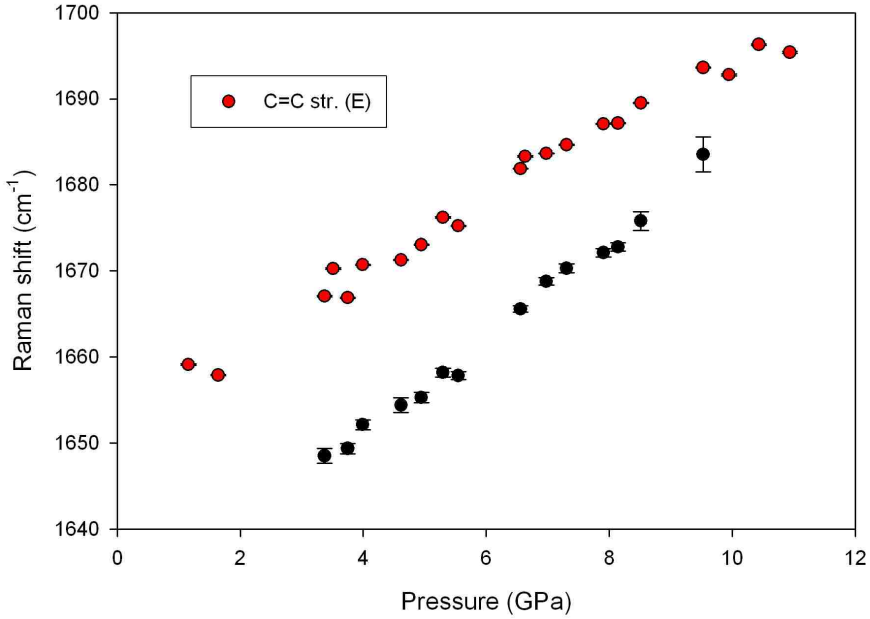

Figure 22. C=C stretching region (Raman).

Aromaticity

Aromaticity as defined requires that a cyclic molecule be planar. Although the data might not suggest a planarization over pressure, it can separately address the issue of bond distance equalization along the carbon ring as required by aromatization. This equalization necessitates that the C=C double bonds transform into C-C single bonds over pressure, as an electron in the double bond delocalizes to the entire carbon ring. A smooth, continuous transformation would likely see a progressive softening of the C=C vibrational modes over pressure, as it approaches the weaker energy of vibration of the single carbon bond (C-C) vibration.

This softening effect is not manifest in the data, as shown by Figure 23, wherein the C=C bonds instead smoothly increase in energy over pressure, until two of the identified modes disappear. Their disappearance, on the other hand, might suggest sudden aromatization, where electron delocalization (and hence bond equalization along the ring) occurs abruptly with pressure. With the sudden loss of the molecular C=C bonds (having turned into C-C bonds), it is plausible that the corresponding vibrational peaks also disappear. Although if this were the case, the C=C stiffening still needs to be addressed, as a mode softening seems to provide a more self-consistent process preceding an abrupt delocalization than does mode stiffening.

It should also be noted that the modes might not be disappearing at all, but are attenuated under pressure to the point of being undetectable within the limits of the detector.

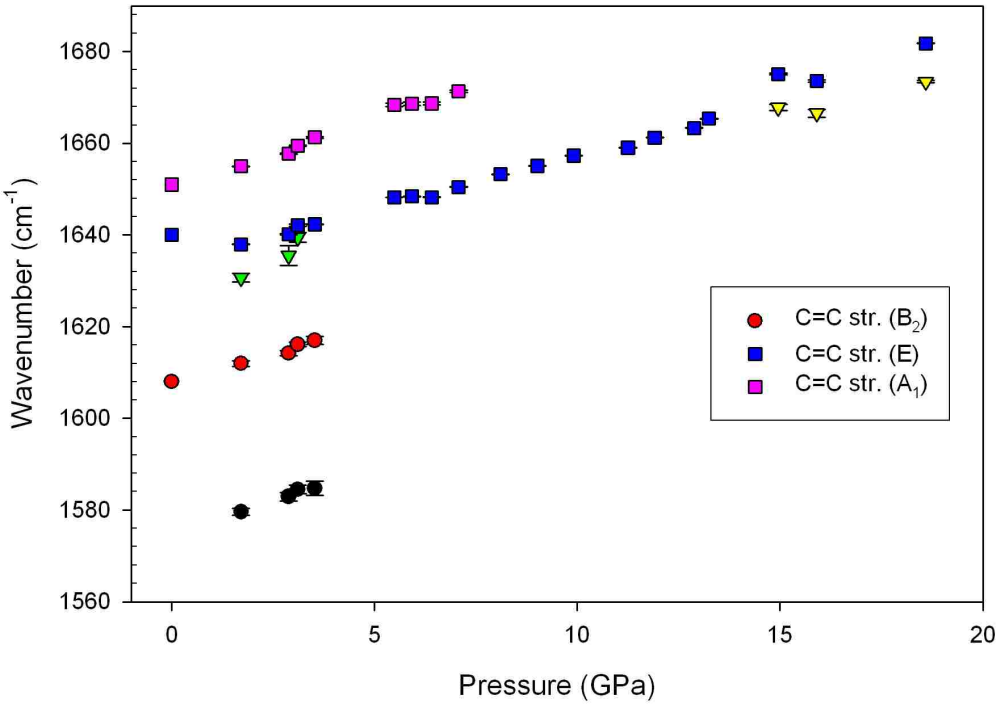

Figure 23. C=C stretch region (MidIR).

Additionally, the pure C-C=C bending vibration in Figure 24 and perhaps the C-C=C + ring torsion vibration in Figure 25 should display the same hypothesized softening over increasing pressure, if both molecular planarization and bond equalization were to take place. This would cause the bond angles inside the carbon ring to approach those of an octagon (135°), as opposed to the zero pressure molecular equilibrium structure angle of ~127° [1]. Along with the lengthening of the C=C bonds, the force constants for vibrations within the ring should decrease with greater separation between the carbon atoms. However, as the data shows, no mode softening of the bending vibration is indicated, which further lends against the hypothesis of molecular aromatization.

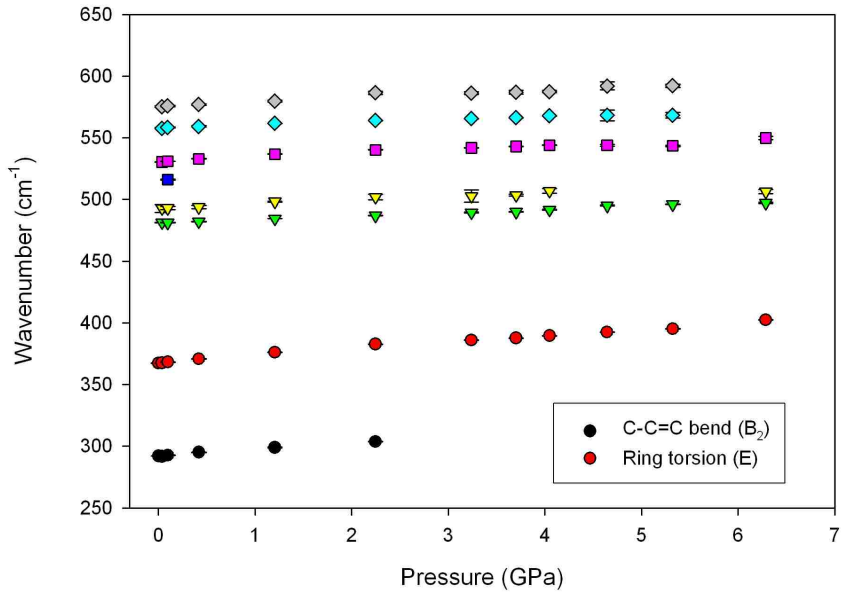

Figure 24. FarIR region.

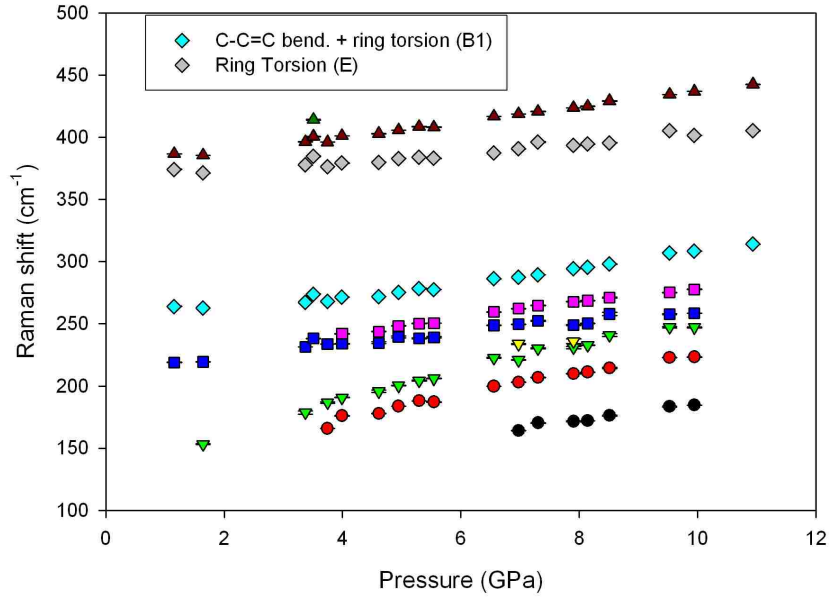

Figure 25. Low-frequency region (Raman).

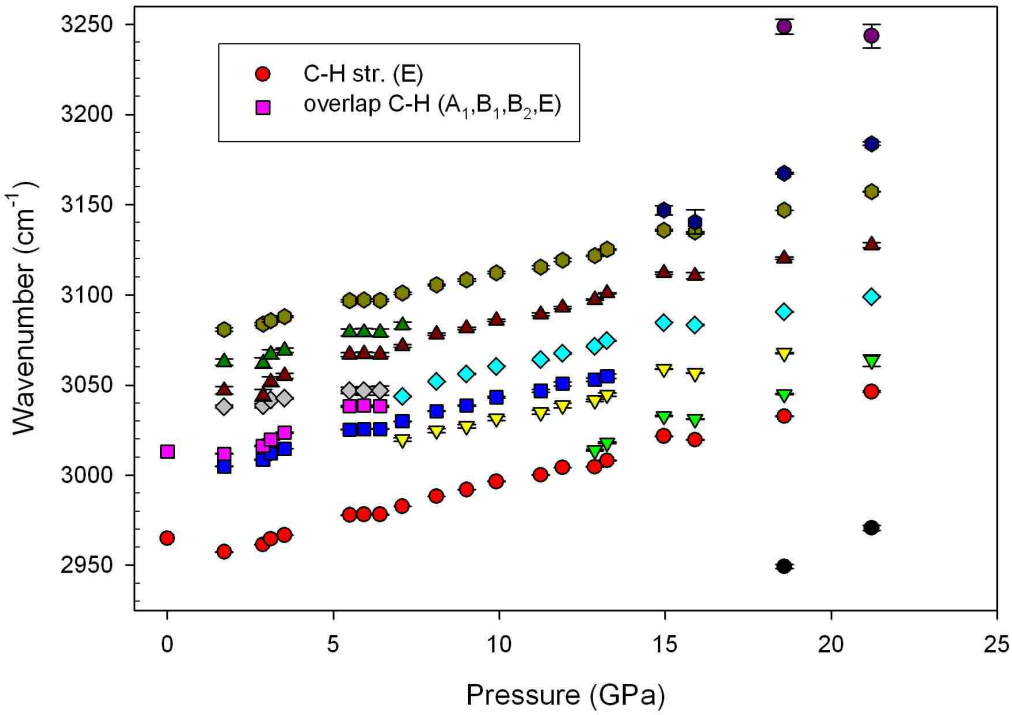

Figure 26. C-H stretching region (MidIR).

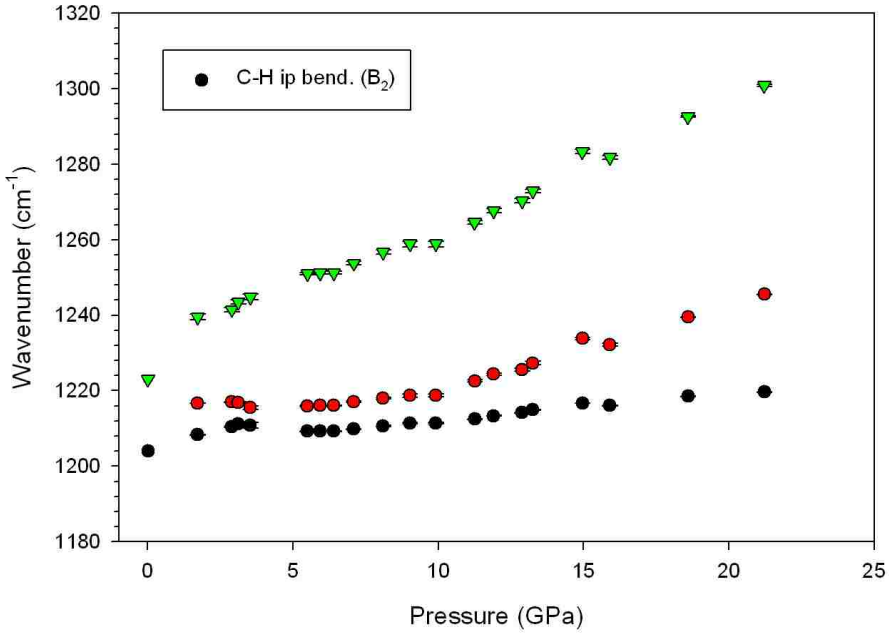

Figure 27. C-H ip bending mode (MidIR).

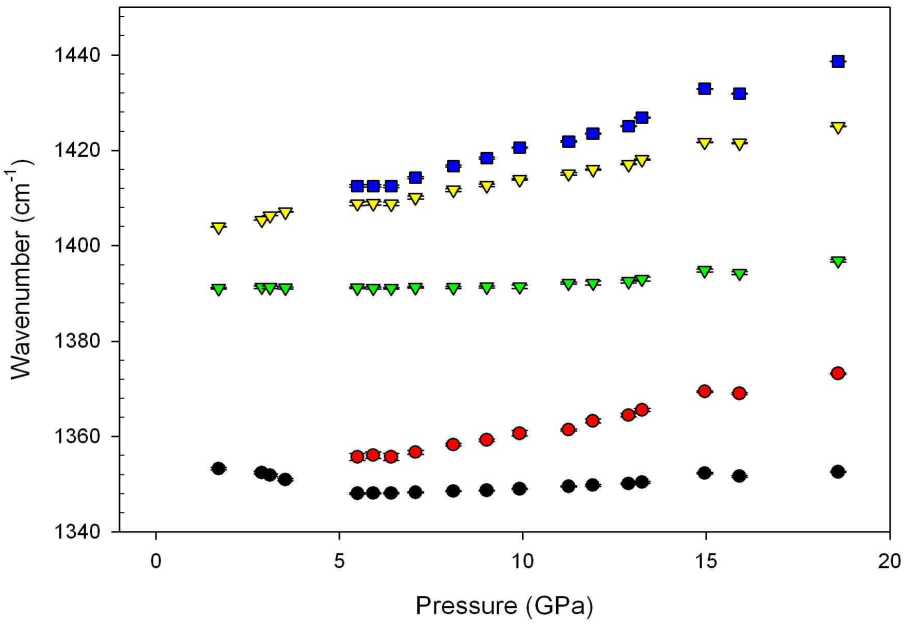

Figure 28. Unassigned region (MidIR).

***This page contains plots unreferenced in the text. They are included for completion.

Phase transition

Another goal of this work was to confirm the findings of Ref. 12, where a crystallographic phase transition to the low temperature phase Aba2 of COT (Figure 2) given by Ref. 1 was possibly observed to occur in the range of 6-12 GPa at room temperature. The splittings of the zero-pressure doubly-degenerate vibrational E modes are consistent with this finding, although not strongly suggestive, since any other space group that lowers the symmetry of the system will also cause the peak splitting. Nevertheless, these splittings occur all throughout the data (see E modes in Figures 19-26), and deserve some mention.

To make sense of the splittings, the correlation diagram for the low temperature phase is given in Figure 29, which shows that the E mode splitting is due to the site symmetry effect. The correlation diagram was constructed using Ref. 27. The diagram shows how the symmetry species that describe the vibrations change from the free molecule (D_{2d} group symmetry) to its placement into a C_2 site group symmetry environment and finally into a the unit cell environment (represented by the factor group symmetry D_{2v}). The diagram reveals that the E mode symmetry under the molecular point group splits into two one-dimensional irreducible representations (symmetry species) A and B under the site group perturbation. This splitting is manifest in most of the data as either an identifiable doublet or an asymmetry of the peak tracked as an E mode (for the free molecule). One E mode, the ring torsion mode in Figs. 24 and 25 shows no splitting, limited of course by the available instrumental resolution.

It should also be considered that the strain induced by the perceptible pressure

gradient across the sample would also induce symmetry-breaking of the E modes. However, an order of magnitude estimate of the PV work done on the sample by a maximal strain of 5 GPa over a sample volume of 72000π μm^3 (a hole diameter of 120 μm and sample thickness of 20 μm), gives roughly 10^{-3} J. Normalizing this value to the molecule requires division by the number of molecules in the sample volume, which can be estimated by using the low-temperature crystal structure. The normalization factor turns out to be about $1/10^{14}$, giving a value of ~10^{-17} J for the work due to strain, or 6000 kJ/mol.

On the other hand, an estimate of the splitting of $\Delta\tilde{\nu}=50\ cm^{-1}$ gives an energy difference of about 1 x 10^{-21} J, or around 0.6 kJ/mol using $\Delta E=hc\Delta\tilde{\nu}$. But since there are 10 E modes for the free molecule, that gives an energy of 6 kJ/mol. These first-order calculations reveal that splitting due to strain would be about three orders more than the observed splitting in the data, hence the effect of strain on the splittings can be ruled out.

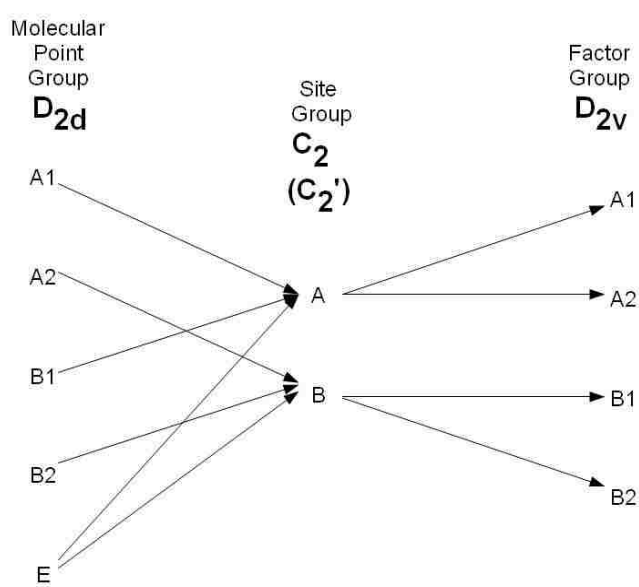

Figure 29. *Correlation Table for low-temp phase of COT. Modes of E symmetry are split by the presence of the C_2 site symmetry.*

Finally, the “amorphous” phase created at high pressure in Ref. 12 is reproduced in this study. The waxy, milky appearance of the substance was observed visually upon opening of the DAC and releasing the sample to air, also as it is in the previous Raman study (Ref. 12). The loss of long-range order presented in the Raman spectra in Ref. 12 is also reproduced in the IR spectra shown in Figures 31 (FarIR) and 33 (MidIR) upon decompression, compared to the quality of the spectra upon compression as shown by Figures 30 (FarIR) and 32 (MidIR). Figure 31 shows the disappearance of the weaker vibrational peaks across the FarIR range after taking the sample to a terminal pressure of ~12 GPa, while Figure 33 shows the sweeping disappearance of the sharp spectral features in Figure 32 across the entire range after being taken to a terminal pressure of ~25 GPa.

The gross broadening of the C-H stretch region in Figure 33 encourages us to draw the parallel with a high-pressure study of benzene, which shows the same effect [28]. Ostensibly, the C-H stretching band of benzene (Figure 34) shows a significant broadening similar to COT under a similar range of pressures. Ref. 28 determines that benzene transforms into a polymer after pressurization to 30 GPa, and the same might be true of COT. This cannot be determined absolutely until the reacted product has undergone chemical analysis, but the study on benzene provides a comparative analogue. The loss of all intermolecular features in Figure 33 except for the broad and intense C-H band is in favor of this interpretation, as the COT molecular ring opens up to cross-link its carbon constituents with those of nearby molecules (making extra C-C single bonds), using up the available bonding electrons from what were once molecular double bonds.

Hence a polymer is made in which C-H stretches still exist in a continuous variety of field environments, broadening the C-H band. Otherwise what else remains are the networked C-C links, having an even broader range of frequencies which probably make up part of the spectral background.

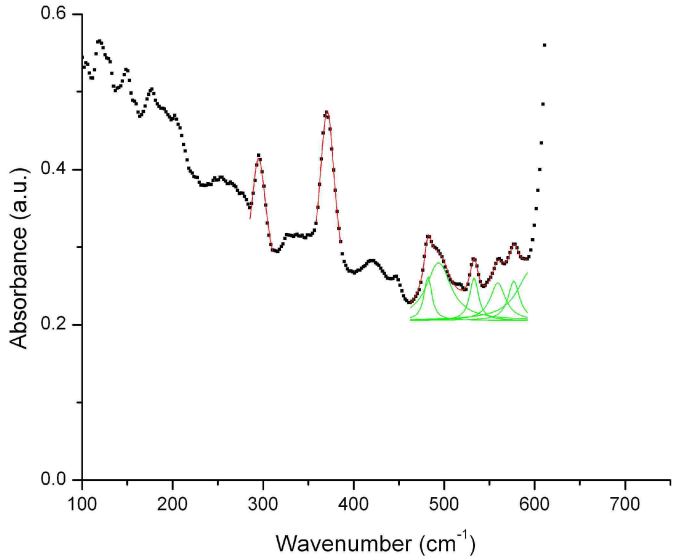

Figure 30. *FarIR spectrum at 0.38 GPa*

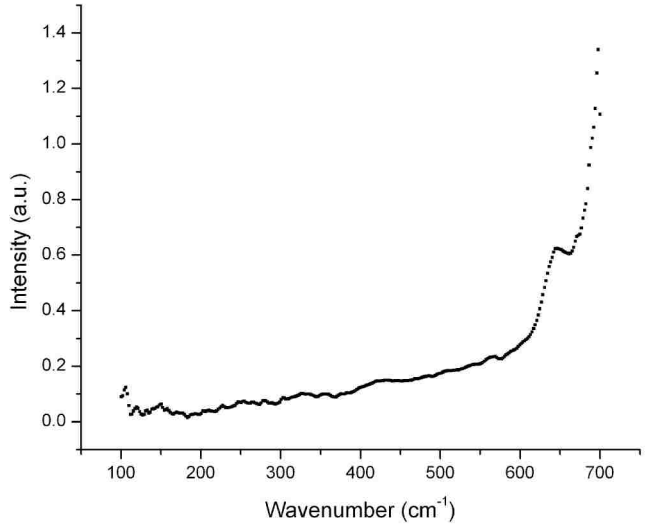

Figure 31. *FarIR spectrum at ~10 GPa.*

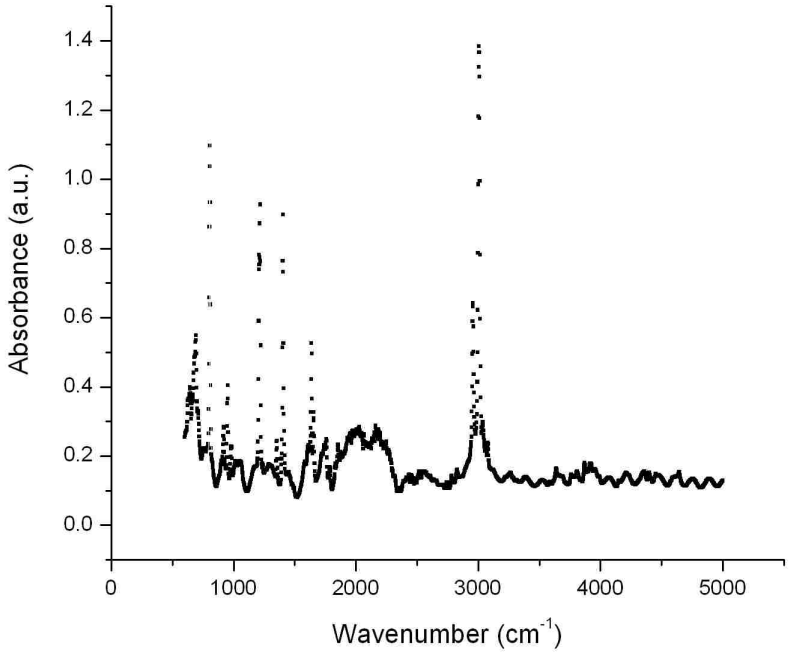

Figure 32. *Entire MidIR spectrum upon compression to 1.59 GPa*

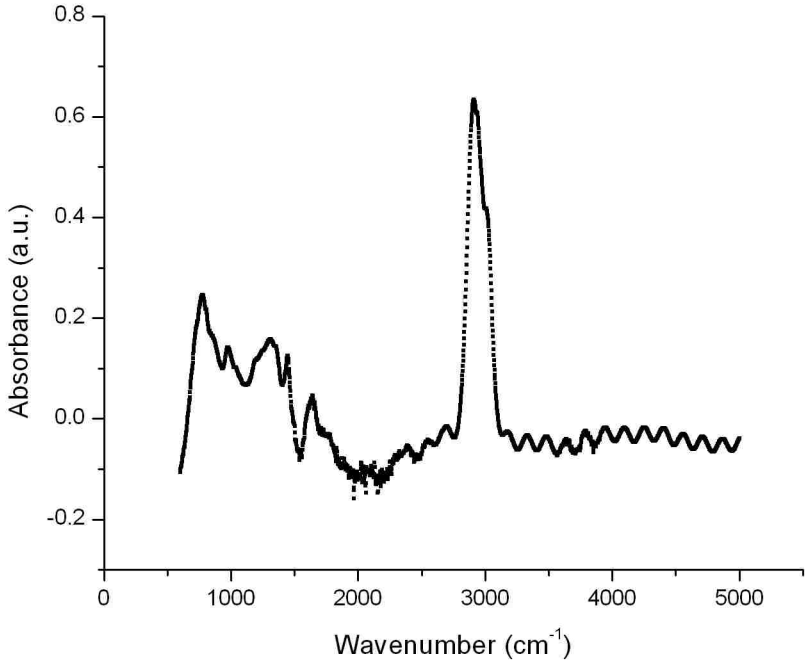

Figure 33. *Entire MidIR spectrum upon decompression to 1.05 GPa.*

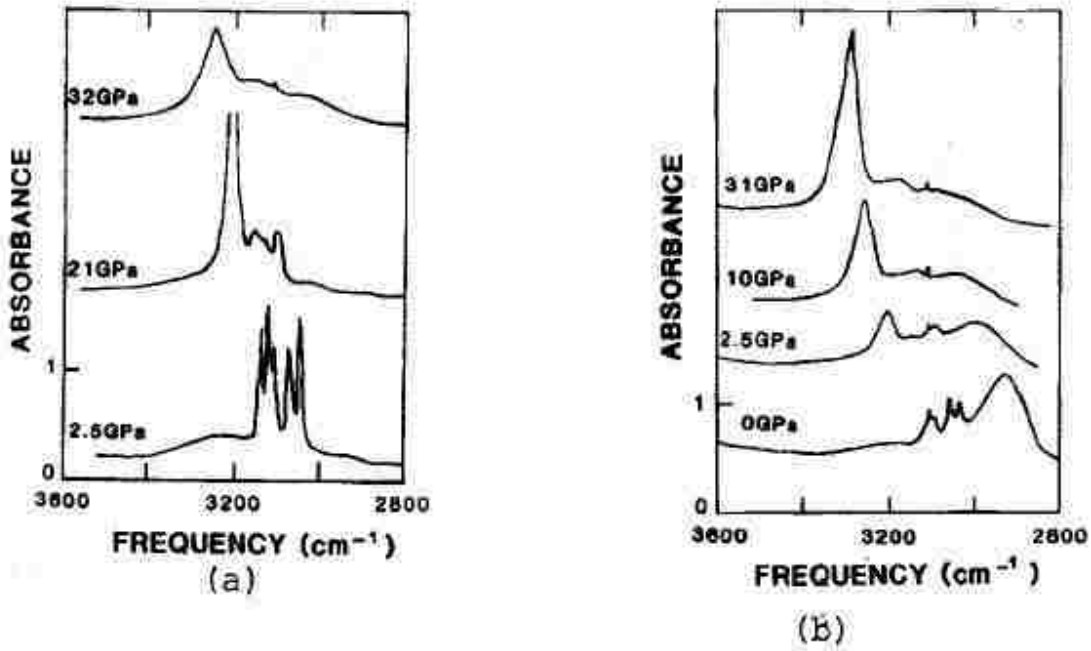

Figure 34. *C-H stretch region IR spectrum of benzene over pressure. a) Benzene under compression. b) Benzene under decompression. Modified from [28].*

CHAPTER 4

CONCLUSIONS

Regarding questions of planarization and aromaticity over pressure, the data shows evidence that this is probably not the case up to the pressures we studied. A continuous transformation from the D_{2d} tub-structure of the COT molecule to the hypothesized D_{8h} planar structure would predict certain modes to soften under increasing pressure, which the data does not provide.

Peak splittings of the free molecule's degenerate E modes are observed in the data. The correlation diagram for the low-temperature phase determined by Ref. 1 indicates that this would be due to the site group effect if the crystal phase occurring at high pressure is indeed the low-temperature structure given in Ref 1. The splittings however offer no strong evidence of the particular crystal phase, as any space group (including the suggested low-temperature Aba2 phase) that lowers the symmetry of the system will cause the splittings. Notwithstanding, the fact that the splittings occur fails to rule out the Aba2 phase as the structure of the solid at the 6-12 GPa pressure regime as suggested in Ref. 12.

As far as determining the actual phase into which COT transforms, single crystal x-ray diffraction should be conducted on the sample. We have acquired x-ray powder data on COT over pressure in the past, but the resultant x-ray images indicate poor powder statistics through non-uniform diffraction rings. This is largely due to the fact that COT is loaded as a fluid at ambient pressure and then naturally crystallizes into a polycrystalline sample over pressure instead of a powder. Marginal improvements to the “powder” x-ray

quality has been achieved by loading silica aerogel into the sample chamber to act as a multi-site seed crystal, encouraging the growth of more independent crystal sites to enhance statistics. This would however be another challenge for an IR study as silica is apparently a strong absorber of radiation in the IR range. Nevertheless, a single-crystal x-ray study would offer the most definitive approach in solving the crystallographic structure.

Visual observation of what might be polymerized COT, which does not evaporate like liquid COT, is another result of the experiment, achieving chemistry induced by high pressure (~25 GPa). Comparison with benzene shows a similar behavior in its IR spectrum under decompression. Although, this comparison is purely suggestive; chemical characterization must be performed on the produced material to be certain. But there are definite qualitative similarities, such as its resistance to melting under heat and the description of a "milky, brittle solid" [28].

REFERENCES

[1] K.H. Claus and C. Kruger, *Acta Cryst. C*, 9, 132 (1998).

[2] T.M. Krygowski, E.P. Pindelska, M.K. Cyrański, and G. Häfelinger, Chem. Phys. Lett., 359, 158 (2002).

[3] O. Castaño, R. Palmeiro, L.M. Frutos, and J. Luisandrés. J. Comput. Chem., 23, 732 (2002).

[4] F.A.Lanet, A.J.R. Bourn, and Y.S. Lin, J. Am. Chem. Soc., 86, 3576 (1964).

[5] C.D. Stevenson, E.C. Brown, D.A. Hrovat, and W.T. Borden. J. Am. Chem. Soc., 120, 8864 (1998).

[6] J.H. Hammons, D.A. Hrovat, and W.T. Borden, J. Am. Chem. Soc., 113, 4500 (1991).

[7] T. J. Katz, J. Am. Chem. Soc., 82, 3784 (1960).

[8] L.A. Paquette, T. Wang, and C.E. Cottrell, J. Am. Chem. Soc., 109, 3730 (1987).

[9] E. R. Bernstein et al., J. Chem. Phys., 48, 5596 (1968).

[10] L. Ciabini et. al., Phys. Rev. B, 72, 094108 (2005).

[11] M.M. Thiery and J.M. Leger, J. Chem. Phys., 89, 4255 (1966).

[12] S.N. Tkachev, M.P. Pravica, E. Kim, E. Romano, and P.F. Weck, J. Phys. Chem. A., 112, 11501 (2008).

[13] G.J. Piermarini, S.Block, J.D. Barnett, and R.A. Forman, J. Appl. Phys., 46, 2774 (1975).

[14] K. Syassen. High Press. Res., 28, 75 (2008).

[15] W.F. Sherman and G.R. Wilkinson, "Raman and Infrared Studies of Crystals at Variable Pressure and Temperature." Advances in Infrared and Raman Spectroscopy, chapter 4, Heyden & Son, 1980.

[16] D.C. Harris and M.D. Bertolucci, Symmetry and Spectroscopy: An Introduction to Vibrational and Electronic Spectroscopy, chapter 3, Oxford University Press, 1978.

[17] J.R. Ferraro, K. Nakamoto, and C.W. Brown, Introduction to Raman Spectroscopy,

chapter 1, Academic Press, 2003.

[18] S.P. Davis, M.C. Abrams, and J.W. Brault, Fourier-Transform Spectroscopy, chapter 3 and 6, Academic Press, 2001.

[19] P.R. Griffiths and J.A. de Haseth, Fourier-Transform Infrared Spectrometry, chapter 5, John Wiley & Sons, 1986.

[20] W. Winick, Synchrotron Radiation Sources: A Primer, chapter 1, World Scientific, 1994.

[21] Z. Liu, J. Hu, H.K. Mao, and R.J. Hemley, J. Phys.: Condens. Matter, 14, 10641 (2002).

[22] M. Eremets, High Press. Exp. Meth, Oxford, 1996.]

[23] B. D. Hosterman, Micro-Raman study of the Corrosion of Stainless Steel by Lead-Bismuth Eutectic, Masters Thesis, University of Nevada Las Vegas, Las Vegas (2008).

[24] D.M. Adams, R. Appleby, and S. K. Sharma, J. Phys. E: Sci. Instr., 9, 1140 (1976).

[25] M. Galley, Micro-raman spectroscopy of 1,3,5,7-cycoloctatetraene, Unpublished raw data (2008).

[26] M. Perec. Spectrochimica Acta, 47A, 799 (1991).

[27] W.G. Fateley, F.R. Dollish, N.T. McDevitt, and F.F. Bentley, Infrared and Raman Selection Rules for Molecular and Lattice Vibrations: The Correlation Method, chapter 1 and 2, John Wiley & Sons, 1972.

[28] P. Pruzan, J.C. Chervin, M.M. Thiéry, J.P. Itié, J.M. Besson, J.P. Forgerit, M. Revault, High Press. Res., 3, 215 (1990).

[29] Zhuravlev, K.K. And McCluskey, M.D. J. Chem. Phys., 117, 3748 (2002).

VITA

Graduate College
University of Nevada, Las Vegas

Edward Don M. Romano

Degrees:
Bachelor of Science, Computational Physics, 2007
University of Nevada, Las Vegas

Special Honors and Awards:
UNLV McNair Scholar
NSF-EPSCoR 2006-2007 Academic Year Grant Awardee

Publications:
"High pressure infrared study of 1,3,5,7-cyclooctatetraene (COT)," M. Pravica, **E. Romano**, S. Tkachev, Z. Liu, accepted for publication in the AIRAPT conference proceedings, *Journal of Physics: Conferences Series* (**2009**).
"High Pressure Studies of 1,3,5,7 Cyclooctatetraene: Experiment and Theory," S. Tkachev, M. Pravica, E. Kim, **E. Romano**, P. Weck, *Journal of Physical Chemistry A* 112, pp. 11501-11507 (**2008**).
"High Pressure Studies of Cyclohexane to 40 GPa," M. Pravica, YR Shen, Z. Quine, **E. Romano** and D. Hartnett, *Journal of Physical Chemistry B*, 111, 4103-4108 (**2007**).
"X-ray diffraction study of elemental thulium at pressures up to 86 GPa," M. Pravica, Z. Quine, **E. Romano**, *Physical Review B*, 74, 104107 (**2006**).
"X-ray diffraction study of elemental erbium to 70 GPa," M.G. Pravica, **E. Romano** and Z. Quine, *Physical Review B*, Volume 72, 214122 (**2005**).

Thesis Title: Vibrational Spectroscopic Study of 1,3,5,7-Cyclooctatetraene at High Static Pressures

Thesis Examination Committee:
Chairperson, Michael Pravica, Ph. D.
Committee Member, Lon Spight, Ph. D.
Committee Member, Oliver Tschauner, Ph. D.
Committee Member, Len Zane, Ph. D.
Graduate Faculty Representative, Clemens Heske, Ph. D.